frontiers in Mechanical Engineering

TYPE Original Research
PUBLISHED 22 July 2026
DOI 10.3389/fmech.2026.1810068

Check for updates

OPEN ACCESS

EDITED BY
Marcel Ilie,
Georgia Southern University,
United States

REVIEWED BY
Ngnassi djami Aslain Brisco,
University of Ngaoundéré, Cameroon
Delanyo Kwame Bensah Kulevome,
Qilu Institute of Technology (QIT), China
Hao Wang,
Nanjing University of Aeronautics and
Astronautics, China

*CORRESPONDENCE
Nima Rezazadeh,
Nima.Rezazadeh@unicampania.it

RECEIVED 12 February 2026
REVISED 01 May 2026
ACCEPTED 04 June 2026
PUBLISHED 22 July 2026

CITATION
Rezazadeh N, De Luca A, Lamanna G, Annaz F and De Oliveira M (2026) Interpretable physics-guided data augmentation for rotating machinery using empirical wavelet transform and sparse identification of nonlinear dynamics.
Front. Mech. Eng. 12:1810068.
doi: 10.3389/fmech.2026.1810068

Interpretable physics-guided data augmentation for rotating machinery using empirical wavelet transform and sparse identification of nonlinear dynamics

Nima Rezazadeh[1,2]*, Alessandro De Luca[1], Giuseppe Lamanna[1], Fawaz Annaz[2] and Mario De Oliveira[2]

[1]Department of Engineering, University of Campania "L. Vanvitelli", Aversa, Italy, [2]School of Architecture, Built Environment, Computing and Engineering, Birmingham City University, Birmingham, United Kingdom

Data scarcity limits the development of machine-learning-based fault diagnosis systems for rotating machinery, especially under noise and varying operating conditions. This paper presents an interpretable, physics-guided data augmentation framework in which empirical wavelet transform (EWT), time-delay embedding and sparse identification of nonlinear dynamics (SINDy) are combined so that the SINDy-identified equations serve not for prediction or control, but as a compact generative model that is perturbed to produce physically consistent synthetic vibration trajectories. Vibration signals are decomposed by EWT into noise-reduced, fault-sensitive modes, embedded in higher-dimensional state space, and governed by compact equations identified via SINDy. Synthetic trajectories generated by perturbing initial conditions preserve fault-related nonlinear features. The framework is evaluated on an experimental broken rotor bar test rig and a numerical rotor-bearing-disc finite element model. Across torsional loads from 1 to 4 N m and rotational speeds from 85 to 115 rad/s, the method contributes to classification accuracies between 95.6% and 100% using augmented data from 1-3 real observations per fault class. Results indicate that combining adaptive signal decomposition with parsimonious dynamical modelling enables effective data synthesis at 10 dB SNR for the tested rotor systems, offering an interpretable alternative to black-box generative models in similar applications.

KEYWORDS
empirical wavelet transform (EWT), nonlinear rotor dynamics, physics-guided data augmentation, rotating machinery fault diagnosis, sparse identification of nonlinear dynamics (SINDy)

1 Introduction

Advanced data-driven and learning-based schemes have been reported to improve fault diagnosis in nonlinear machinery such as rotor assemblies (Xu et al., 2025; Li et al., 2020; Torzoni et al., 2025; Rezazadeh et al., 2026a; Rezazadeh et al., 2026b). The translation to large-scale industrial deployment has been impeded by the scarcity of suitable observational datasets (Das et al., 2023; Leite et al., 2024). Limited data have been shown to undermine generalisation and to increase the risk of overfitting in machine learning (ML) classifiers (Rezazadeh et al., 2025; Gharehbaghi et al., 2023; Fallahy et al., 2025).

A common response to data scarcity has been the augmentation of small datasets with synthetic signals generated by physics-based or data-driven models (Zheng et al., 2024; Kumar and Tiwari, 2024). Numerical simulations can omit subtle practical factors such as boundary condition variability, installation effects, and sensor noise, which can introduce a distribution shift between synthetic and real measurements and reduce transferability (Uh et al., 2023). Augmentation strategies should ideally retain physically meaningful dynamics, demonstrate resilience to certain operational variabilities (OVs), and remain interpretable. Sparse system identification has been considered attractive in this regard because it can capture essential dynamics with minimal parameterisation and provide low-order models that can be perturbed and integrated to generate additional, physically consistent trajectories for data augmentation (Naozuka et al., 2022).

Recent studies have combined partial real measurements with model-derived information to improve realism and diversity under practical operating changes (Rezazadeh et al., 2026c). Domain adaptation (DA) has been used to reduce the mismatch between synthetic and real data when available labels are limited (Bai et al., 2024). In rotor systems, time-frequency decompositions, in particular the empirical wavelet transform (EWT), have been used to isolate fault-relevant content by decomposing vibration into frequency-specific components. This procedure has been observed to preserve nonlinear behaviour while mitigating noise, which can provide more dependable inputs for downstream diagnosis (Huang et al., 2020). However, these works use EWT primarily as a feature extractor, not as the basis of a generative model.

A physics-guided augmentation framework is introduced in this work in which sparse, interpretable ordinary differential equations (ODEs) are identified from EWT components of a real vibration observation using sparse identification of nonlinear dynamics (SINDy). Synthetic trajectories are then produced by applying controlled perturbations to initial conditions of the identified ODEs. In this way, fault-specific nonlinear dynamics are retained while realistic variability in operating conditions and noise is reflected. The approach is aimed at rotor systems for which EWT isolates fault-relevant content and for which SINDy identifies compact governing relations from limited data. The framework is evaluated on one experimental and one numerical rotor platform, which reflects the practical boundaries of the available datasets for this study.

Whereas prior studies have employed SINDy for system identification, control design, and fault detection (Brunton et al., 2016; Lee et al., 2024; Piramoon et al., 2024; Zhao et al., 2024a; Bhadriraju et al., 2022), and EWT as a pre-processing or feature-extraction stage (Zheng et al., 2017; Zhang et al., 2019a; Xin et al., 2019; Yan et al., 2023), the present work assigns a distinct role to these established tools: the SINDy-identified equations are used not for prediction or control, but as a compact, perturbable generative model from which physically consistent synthetic vibration trajectories are produced for data augmentation. Within the context of rotating machinery fault diagnosis, this repurposing enables the generation of synthetic fault data from as few as a single real observation per operating condition; that is, a generative application of the EWT-SINDy pipeline that has not been explored in previous work on rotating machinery fault diagnosis.

1.1 Main contributions

The principal additions to the field under conditions of limited observations are summarised below.

i. Physics-guided augmentation from a single real observation per condition is shown to preserve fault-specific nonlinear behaviour and to support strong classification performance under noise and OVs.
ii. Applicability across operating conditions is demonstrated through validation on an induction-motor experiment with varying loads and on a FE rotor-bearing-disc model at different speeds, suggesting potential for broader application to rotary machinery pending further validation.
iii. Performance under noisy conditions is characterised by reporting results across load and speed settings, single-seed and multi-seed synthesis, and SINDy sparsity levels.
iv. Comparative advantage and interpretability are established by outperforming data augmentation benchmarks under matched data conditions, and by using sparse equations to explain outcomes and to diagnose reconstruction or sensor-setup issues.

An interpretable, physics-guided toolkit is presented that addresses data scarcity for the rotor systems tested, with potential applicability to similar rotating machinery configurations.

Table 1 outlines the Abbreviations employed in this paper, providing clear and consistent definitions to maintain clarity and coherence throughout the subsequent technical discussions.

The remainder of this paper is organised as follows. Section 2 reviews related work; Section 3 describes the EWT-SINDy, methodology and modelling details; Section 4 presents the experimental and numerical case studies; Section 5 reports the classification and reconstruction results; Section 6 discusses the implications and robustness of the proposed framework; and Section 7 concludes the paper by outlining its limitations and suggesting directions for future research.

2 Related works

Previous research was conducted to address the challenge of insufficient samples for training ML-based fault diagnosis in rotor and rotating machinery systems through various approaches (Fathnejat and Nava, 2025). Techniques based on the synthetic minority over-sampling technique, such as Cluster-MWMOTE for limited and complex bearing data in rotating machinery (Wei et al., 2020) and related cluster-based schemes for high-dimensional unbalanced rolling bearing data (Hang et al., 2019), were proposed to enhance sample diversity and to tackle the imbalance present in fault diagnosis datasets. Generative models, particularly those based on deep learning (DL), such as deep convolutional generative adversarial networks that were applied to rolling bearing assemblies and sliding bearing-rotor systems in

TABLE 1 Abbreviation list.

Acronym	Full term
ACGAN	Auxiliary classifier generative adversarial network
AWGN	Additive white Gaussian noise
CNN	Convolutional neural network
DA	Domain adaptation
DL	Deep learning
EMD	Empirical mode decomposition
EWT	Empirical wavelet transform
FE	Finite element
GAN	Generative adversarial network
IFFT	Inverse fast fourier transform
Mixup-DA	Mixup-based data augmentation
ML	Machine learning
ODEs	Ordinary differential equations
OVs	Operational variabilities
PCA	Principal component analysis
RMSE	Root mean square error
SINDy	Sparse identification of nonlinear dynamics
SNR	Signal-to-noise ratio
VAE	Variational autoencoder

nuclear power plant applications (Radford et al., 2016; Zhu and Fang, 2024; Li et al., 2024a), were developed to produce synthetic signals that closely resembled real rotating machinery vibration responses. Similarly, Wasserstein GANs with gradient penalty were employed for aero-engine, rolling bearing and centrifugal pump fault diagnosis in turbomachinery and rotating equipment, thereby enabling improved synthetic data generation for these systems (Zhao et al., 2019; Pei et al., 2022; Li et al., 2024b). Variational autoencoder (VAE) frameworks, including conditional VAE for rotary machines with few samples (Dixit and Verma, 2020) and semi-supervised Gaussian mixture VAE for few-shot fine-grained fault diagnosis in industrial machinery (Zhao et al., 2024b), were adopted to provide controlled and statistically consistent synthetic data.

Data transformation and auxiliary representation methods that were beneficial for augmenting vibration or derived visual data in rotating machinery, such as correlation-based feature construction for health perception in rotating machines (Zhang et al., 2019b) and noise-enhanced Siamese architectures for imbalanced planetary gearbox diagnosis (Zhang et al., 2023a), were introduced to manipulate existing data into new variants and thereby enrich the training landscape for fault diagnosis models. These approaches collectively widened the scope and depth of available training samples in rotating machinery and turbomachinery applications and were reported to support more robust, accurate and generalisable fault diagnosis. However, these methods were formulated as data-driven schemes rather than physics-guided generators, and governing equations of motion were not identified; as a result, the vibration signal was treated as a pattern to be replicated instead of as the realisation of an underlying dynamical system, while issues such as potential overfitting, the introduction of biases and high computational demands still required careful management.

Numerical simulations, including finite element (FE) and analytical modelling approaches, together with experimental prototypes, were widely adopted to address data scarcity in rotor and rotating machinery fault diagnosis. A common strategy was the use of FE-generated vibration responses to train ML models (Rezazadeh et al., 2023). In one representative study, Zhang et al. applied FE-based transfer learning (Zhang et al., 2023b) in order to generate synthetic rotor fault data and to improve classification performance, with Fourier and wavelet transformations being used for feature extraction. Similarly, unsupervised deep transfer learning with simulated rotor samples was investigated by Xiang et al. (2023), in which adversarial learning was incorporated to reduce domain discrepancies between source and target domains. Analytical models were also constructed to simulate rotor or turbomachinery behaviour. For instance, Jiang et al. proposed an orbit-based augmentation strategy (Jiang et al., 2024) to improve transferability in turbomachinery diagnostics, where simulated orbit images from analytical models were treated as source-domain data and combined with real sensor measurements as target-domain data for dynamic feature extraction. Beyond simulation-based augmentation, DA techniques were applied to vibration data obtained from disparate test rigs. Cao et al. presented an unsupervised adversarial DA network (Cao et al., 2022), in which feature alignment between synthetic and real rotor data was enhanced through clustering-based refinement. Further expansion of hybrid strategies was provided by Rezazadeh et al. (2024), where wavelet transformation, transformer encoders and multi-layer perceptrons were combined, followed by fine-tuning, to improve generalisation across operating conditions. Although these approaches were effective in mitigating data scarcity, they depended on large sets of simulated or multi-rig measurements and on explicit DA stages, rather than on a compact physics-guided generator that was learned directly from a small number of measured vibration signals.

Despite these advancements, three key challenges were still observed: (i) a persistent need for DA to correct feature distribution mismatches between synthetic and real-world data, (ii) high computational costs, particularly in DL-based methods, and (iii) the requirement for extensive model calibration in order to ensure that simulated fault responses remained dependable for practical industrial applications.

EWT was extensively validated as a robust and versatile pre-processing and feature extraction tool in rotor and rotating machinery fault diagnosis, owing to its capacity to adaptively decompose complex, non-stationary vibration signals into intrinsic modes that revealed critical fault features. An adaptive, parameterless EWT framework was, for example, employed to isolate and enhance key components associated with rotor rubbing faults (Zheng et al., 2017), while fractional extensions of EWT were shown to provide superior separation of overlapping frequency-modulated components during rotor start-up conditions (Zhang et al., 2019a). Comprehensive reviews and adaptive reinforcement strategies were also reported to demonstrate the strengths of EWT in capturing the nuanced dynamic behaviour of rotor systems (Xin et al., 2019; Yan et al., 2023). In these studies, EWT was primarily adopted as a pre-processing or feature extraction stage and was not used to construct generative dynamical models that could be perturbed in order to produce physics-consistent synthetic vibration signals.

Sparse system identification techniques such as SINDy were increasingly implemented in control systems, structural health monitoring and robotics, because underlying dynamics were captured from limited data and were then used for accurate modelling, prediction and improved system performance. SINDy was initially introduced by Brunton et al. (2016) for the extraction of governing equations of nonlinear dynamical systems directly from measurement data by means of sparse regression. The effectiveness of SINDy in mechanical fault diagnosis was demonstrated in multiple recent studies. In quadrotor applications, SINDy was integrated with a Thau observer by Lee et al. (2024) so that complex nonlinear dynamics, including gyroscopic and aerodynamic effects, were captured and timely fault isolation was enabled. In rotating machinery, SINDy was employed by Piramoon et al. (2024) to model the nonlinear dynamics of vertical shaft rotary machines, and the resulting equations were used as the basis for terminal sliding mode control that suppressed vibrations. The methodology was further extended by Zhao et al. (Zhao et al., 2024a), in which the identified governing equations were embedded into a physics-constrained hybrid network in order to detect breathing cracks and to obtain interpretable, closed-form dynamic models. In addition, a fault prognosis toolkit named OASIS-P was developed by Bhadriraju et al. (2022) by combining SINDy modelling with DL and risk-based process monitoring. Collectively, these studies indicated that SINDy was a versatile tool for extracting accurate and decipherable models from limited data for robust fault diagnosis and control in complex mechanical systems, although it was primarily used for system identification and decision support rather than as a generator of synthetic vibration trajectories.

Recent extensions of SINDy were specifically designed to address the original method sensitivity to noise and to limited state descriptions. Ensemble-SINDy (Fasel et al., 2022) was proposed, in which bootstrap aggregating was used to combine multiple SINDy models and to enhance robustness in low-data, high-noise settings, while Bayesian-SINDy (Fung et al., 2025) recast the identification problem within a probabilistic framework so that uncertainty quantification and improved parameter estimation under noisy conditions were provided. DL based adaptations, such as SINDy-SHRED (Gao et al., 2025) and related architectures with learned coordinate transformations and recurrent decoders (Champion et al., 2019; Faraji et al., 2025), were then introduced to capture latent dynamics in high-dimensional systems, but these variants required larger training datasets, involved increased computational complexity and tended to reduce the transparency of the extracted equations. Variational formulations (Conti et al., 2024) were also reported to broaden the applicability of SINDy to noisy environments, whilst similar challenges remained regarding data requirements and model interpretability. In the context of rotating machinery fault diagnosis with scarce labelled observations, it was therefore considered appropriate in the present work to retain the standard SINDy formulation. Specifically, the present application requires generating synthetic trajectories from as few as one observation per operating condition, a regime in which deep-learning-based SINDy variants would lack sufficient training data, ensemble methods would have no meaningful bootstrap diversity, and Bayesian formulations would offer uncertainty quantification at the cost of additional computational overhead without commensurate benefit for the augmentation objective. The standard formulation was therefore deemed most appropriate for maximising interpretability and minimising complexity from very few seed observations, whilst still exploiting sparse model structure for physically consistent data synthesis.

Recent intelligent maintenance studies further show that industrial diagnosis and prognosis are increasingly being addressed through data-driven, statistical, and reliability-oriented frameworks. Deep-learning-based approaches have been used for integrated diagnosis and prognosis of dynamic industrial systems using multivariate sensor data (Ngnassi Djami and Abdelhakim, 2026), while swarm-intelligence methods have been applied to failure diagnosis and prognosis in production equipment (Ngnassi Djami et al., 2024a). Statistical monitoring approaches, such as Hotelling's T^2 distance and average run length analysis, have also been used to detect process drift in manufacturing systems (Abdelhakim et al., 2025). In parallel, reliability- and dependability-oriented studies have explored evolutionary meta-modelling, stochastic optimisation, and Weibull-based reliability modelling for maintenance decision support in industrial assets (Ngnassi Djami and Nzié, 2025; Djami et al., 2026; Ngnassi Djami et al., 2024b). These studies highlight the growing role of intelligent maintenance and reliability analytics; however, they focus on diagnosis, prognosis, maintenance optimisation, or reliability modelling rather than physics-guided generation of vibration trajectories from scarce measured observations. The present work addresses this gap by using EWT-filtered signals and SINDy-identified sparse dynamics as an interpretable generative mechanism for rotating machinery fault-diagnosis data augmentation.

Taken together, the above developments suggested that enhanced SINDy methods could markedly improve noise robustness and provide uncertainty quantification, but at the expense of additional demands such as extensive observations for training deep components and a potential loss of interpretability. More broadly, although previous research introduced a range of data synthesis, simulation-based and adaptation techniques to bolster fault diagnosis in rotating machinery, inherent limitations persisted in balancing simulation fidelity, computational efficiency and model clarity. Against this background, the EWT-SINDy framework presented in this paper was designed to combine the adaptive decomposition capabilities of EWT with the parsimonious and interpretable modelling properties of SINDy, so that synthetic vibration signals could be generated directly from measured rotor responses in a manner that retained critical nonlinear fault signatures while remaining data-efficient and physics-guided.

3 Methodology and methods

The proposed EWT-SINDy framework, illustrated in Figure 1, provides a toolkit for addressing data scarcity in intelligent damage detection in rotor systems. This is accomplished through a method

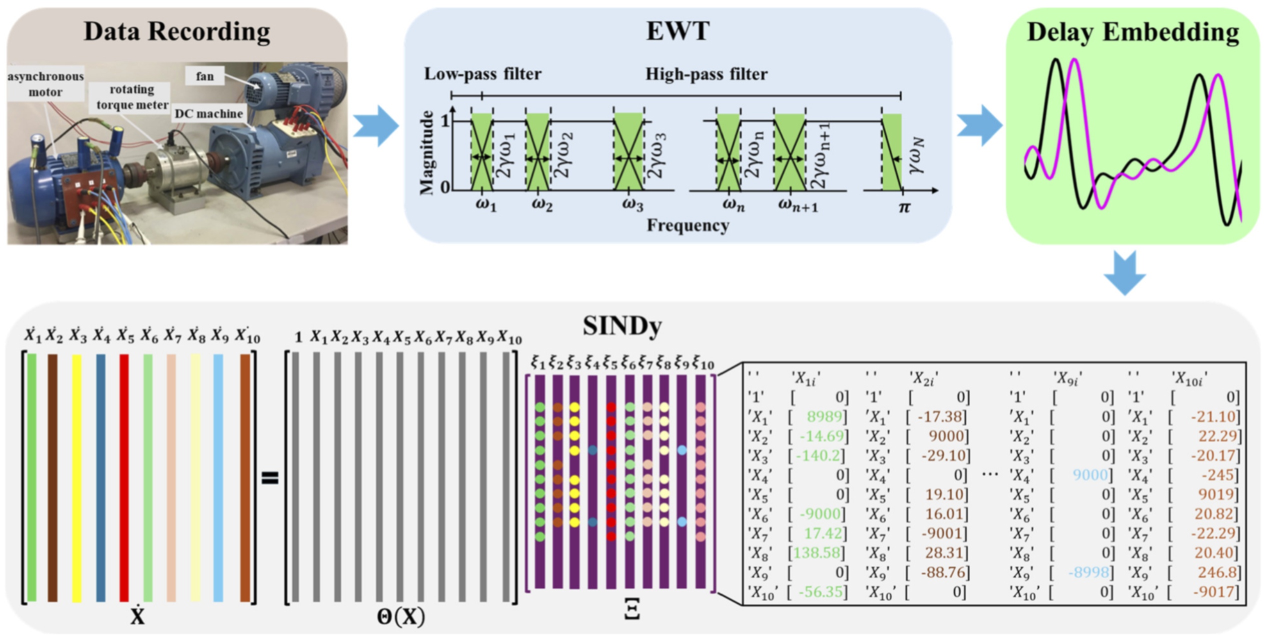

FIGURE 1
Schematic of the EWT-SINDY framework to extract ODEs.

that generates a large set of augmented data based on a single experimental or simulated observation conducted in each health and operational configuration. To this end, EWT was implemented to segment raw vibration signals into distinct frequency bands up to a certain limit; this process helped filter out noise and present dominant fault-relevant features in the data. EWT was preferred to empirical mode decomposition and related approaches because its adaptive filter bank reduced mode mixing and produced smoother, lower-noise modes that were more suitable for sparse equation discovery. Following this, time-delay embedding was implemented to increase the dimensionality of the system, enabling a more detailed description of the time evolution in the signals. Initial experiments compared reconstruction accuracy across embedding dimensions $m \in \{1, 2, 3, 4\}$ and delays $\tau \in \{1, 2, 5, 10\}$ on a subset of training data from the normal condition at T = 2 N m. Results showed that $m = 2$ with $\tau = 1$ achieved the lowest reconstruction RMSE (average 0.12 mm/s) whilst maintaining model parsimony (average 8–12 active terms per equation). Higher values of m and τ marginally improved reconstruction (below 5% RMSE reduction) but increased computational cost (i.e., 3 to 5 times longer training time) and reduced interpretability (20–30 active terms per equation). These values were therefore adopted throughout.

The transformed data, in a higher state space containing the decomposed observations, are then used for system identification via the SINDy algorithm. The approach uncovers the governing ODEs of the embedded EWT coefficients concisely and is intended for regimes where only limited labelled data are available.

Once these sparsely formulated ODEs are set up, the ultimate step in augmentation involves perturbing the initial conditions through controlled variations. By numerically solving the resulting systems, multiple trajectories are generated, each of which traces a variation of the decomposed fault signatures in the initial measurement. The perturbations are chosen to be small relative changes to the initial state, so that the synthetic trajectories remain in a neighbourhood of the observed operating condition and preserve the qualitative dynamics, while still introducing meaningful variability; excessively large perturbations were observed to produce unrealistically distorted or unstable responses and were therefore avoided. The resulting synthetic signals, having realistic variance, are combined with the initial empirical observation to generate a much more expansive training set. In the last phase, features are extracted from the reconstructed EWT coefficients; the resulting feature vectors are used to train various ML models to diagnose faults. Capitalising on the synergistic potential of EWT-based decomposition and SINDy-based data enhancement, the EWT-SINDy method provides a means of dealing with the scarcity of noisy data without compromising the underlying nonlinear dynamics of rotor systems.

3.1 Empirical wavelet transformation

To address the issues of mode mixing in empirical mode decomposition (EMD) and the computational intensity of ensemble EMD, Gilles (Gilles, 2013) introduced EWT, which constructs adaptive wavelets for mode extraction by designing a wavelet filter bank. Unlike conventional wavelet transforms that implement predefined wavelet bases, EWT customises its wavelet filters based on the spectrum of the input signal. It segments the Fourier spectrum to identify significant frequency components and accordingly constructs empirical wavelet filters. To implement an EWT on a vibration signal $x(t)$, 4 consecutive steps ought to be conducted as the following.

1. Segmentation of the Fourier spectrum that can be performed in 3 sub-phases as:

i. Compute the Fourier spectrum $X(\omega)$ of the signal $x(t)$, as defined in Equation 1.

$$X(\omega) = \mathcal{F}\{x(t)\} = \int_{-\infty}^{+\infty} x(t)e^{-j\omega t}dt \tag{1}$$

ii. Identify the locations of local maxima in the Fourier spectrum.

iii. Define segmentation boundaries as the midpoints between successive local maxima.

2. The empirical filter bank is constructed by segmenting the frequency domain into distinct bands. For each segmented band, an empirical scaling function $\hat{\phi}_n(\omega)$ and empirical wavelets $\hat{\psi}_n(\omega)$ are defined. The localised frequency characteristics of the signal are captured by these functions. Specifically, Equation 2 is used to define the empirical scaling function, while Equation 3 is employed to define the empirical wavelet function. Together, the signal is decomposed into its constituent frequency components in a data-driven manner.

$$\hat{\phi}_n(\omega) = \begin{cases} 1, |\omega| \le (1-\gamma)\omega_n \\ cos\left(\frac{\pi}{2\beta}\frac{1}{2\gamma\omega_n}(|\omega| - (1-\gamma)\omega_n)\right), (1-\gamma)\omega_n < |\omega| \le (1+\gamma)\omega_n \\ 0, \text{otherwise} \end{cases} \tag{2}$$

$$\hat{\psi}_n(\omega) = \begin{cases} 1, (1+\gamma)\omega_n < |\omega| < (1-\gamma)\omega_{n+1} \\ cos\left(\frac{\pi}{2\beta}\frac{1}{2\gamma\omega_{n+1}}(|\omega| - (1-\gamma)\omega_{n+1})\right), (1-\gamma)\omega_{n+1} \le |\omega| \le (1+\gamma)\omega_{n+1} \\ sin\left(\frac{\pi}{2\beta}\frac{1}{2\gamma\omega_n}(|\omega| - (1-\gamma)\omega_n)\right), (1-\gamma)\omega_n \le |\omega| \le (1+\gamma)\omega_n \\ 0, \text{otherwise} \end{cases} \tag{3}$$

where ω_n are the identified frequency segmentation points and γ is a parameter controlling the width of the transition region; this parameter should satisfy the criterion given in Equation 4.

$$\gamma < min_n\left(\frac{\omega_{n+1} - \omega_n}{\omega_{n+1} + \omega_n}\right) \tag{4}$$

Moreover, $\beta(x)$ is a smooth function used for transitioning between passbands and can be defined as Equation 5:

$$\beta(x) = \begin{cases} 0, & x \le 0 \,\text{and}\, \beta(x) + \beta(1-x)\,\forall\, x \in [0,1] \\ 1, & x \ge 1 \end{cases} \tag{5}$$

3. The empirical wavelet coefficients are obtained by applying the empirical wavelet filter bank to the Fourier-transformed signal. Specifically, the wavelet coefficients at scale n, i.e., $\mathcal{W}_x(n,t)$ are computed by taking the inverse fast Fourier transform (IFFT) of the product of the Fourier-transformed signal $X(\omega)$ and the empirical wavelet $\hat{\psi}_n(\omega)$. The wavelet coefficients are computed using Equation 6.

$$\text{IMF}_n = \mathcal{W}_x(n,t) = \langle x(t), \hat{\psi}_n \rangle = \text{IFFT}(X(\omega) \cdot \hat{\psi}_n(\omega)) \tag{6}$$

4. The signal is reconstructed by summing the wavelet modes, as shown in Equation 7.

$$x(t) = \sum_{n=1}^{N} \text{IMF}_n(t) \tag{7}$$

where IMF_n are the empirical wavelet coefficients corresponding to different frequency bands.

In the present framework, only the modes associated with the dominant low-frequency content were retained for subsequent modelling, so that the main fault-related dynamics were preserved while high-frequency noise components were suppressed, which was beneficial for the stability of the SINDy identification stage.

3.2 Delay embedding

Delay embedding is pivotal for reconstructing the state space from time-series data to reveal the dynamics of a system. Various methods such as derivative embedding and global principal component embedding have been evaluated in system identification tasks; however, time delay embedding has been widely adopted due to its straightforward application and effectiveness (Tan et al., 2023). In this work, time delay embedding was employed to enhance the dimensional structure of the system. The augmented state vector is constructed using the delay-embedding formulation in Equation 8.

$$X(t) = [x(t), x(t-\tau), \cdots, x(t-(m-1)\tau)] \tag{8}$$

here, τ represents the time delay and m denotes the embedding dimension.

In this work, a low-order embedding was adopted, since preliminary experiments showed that such an embedding improved reconstruction of the system trajectories compared with no embedding, while higher orders increased the complexity of the identified models without offering proportional gains.

3.3 Sparse identification of nonlinear dynamics

SINDy offers a compelling methodology for deriving parsimonious representations of the governing equations directly from experimental or simulated measurements. Consider the dynamical system described by the ordinary differential equation in Equation 9 (Brunton et al., 2016):

$$x(t) = f(x(t)) \tag{9}$$

in which each column of $x(t) \in \mathbb{R}^n$ reveals a state of variable vector of the system and $f: \mathbb{R}^n \to \mathbb{R}^n$ outlines the unknown dynamics. The SINDy approach hypothesises that f can be approximated by a sparse linear combination of candidate functions; to conduct this, the library of candidate functions is constructed as shown in Equation 10.

$$\Theta(x) = [\theta_1(x)\,\theta_2(x)\cdots\theta_m(x)] \tag{10}$$

where each $\theta_m(x)$ is a potential nonlinear function of the state variables. For rotating machinery applications, the candidate library $\Theta(x)$ was constructed using polynomial terms up to a specified order, with the optional inclusion of trigonometric functions $\{\sin(x_i), \cos(x_i)\}$. The polynomial order and the inclusion or exclusion of trigonometric terms were determined during the preliminary calibration of each case study and are reported in the corresponding results sections (Sections 5.1, 5.2). Whilst trigonometric functions are common in rotor dynamics, the EWT pre-processing step decomposes the raw signal into amplitude-modulated intrinsic modes, each capturing a narrow frequency band. This decomposition transfers oscillatory content from the raw signal into the amplitude envelopes of the EWT coefficients, so that the state variables presented to SINDy are no longer explicitly periodic waveforms. Trigonometric candidate functions may therefore become redundant in the embedded coordinate space, a hypothesis that was tested and confirmed during the calibration of both case studies.

After forming the library, the task is then to identify a sparse coefficient matrix $\Xi \in \mathbb{R}^{m\times n}$ as defined in Equation 11.

$$\dot{x}(t) = \Theta(x(t))\Xi \tag{11}$$

In practice, the coefficients are determined by solving the sparsity-promoting optimisation problem in Equation 12.

$$\min_{\Xi} \|\dot{x} - \Theta(x)\Xi\|_2^2 + \lambda\|\Xi\|_1 \tag{12}$$

here λ is a regularisation parameter that balances the trade-off between accurately fitting the observed and reconstructed derivatives of the state variables and minimising the number of active terms in the discovered ODEs.

3.4 The proposed EWT-SINDy framework

In the proposed EWT-SINDy framework, the previously described techniques of EWT-based signal decomposition, time delay embedding, and sparse system identification via SINDy were integrated to generate an enhanced dataset for rotor fault diagnosis. Initially, recorded vibration signals were processed through EWT to segregate and augment fault-relevant features, with the resultant output being denoted as $x_{EWT}(t)$. Subsequently, these transformed signals were advanced to a time-delay embedding stage, thereby expanding the data into a more comprehensive higher-dimensional state space, represented as $X(t)$. During the system identification phase, SINDy was employed to distil the parsimonious representations of the differential equations' coefficients $\dot{X}(t)$. The final phase involved generating synthetic trajectories by perturbing the initial conditions of these differential equations and executing numerical solution of the resultant models. The resulting synthetic-data generation is expressed in Equation 13.

$$X_{\text{synth}}(t) = \text{integrate}\left(\dot{X}(t), X(0) + \Delta X_0\right) \tag{13}$$

where ΔX_0 represents small perturbations to the initial conditions to generate diverse trajectories, chosen such that the synthetic responses remain close to the original operating regime while still exhibiting observable variability.

Algorithm 1 illustrates the EWT-SINDy process along with the corresponding data augmentation.

Input: Recorded vibration signals $x(t)$, Embedding dimension m, Time delay τ, Perturbation parameter ΔX_0, SINDy library of candidate functions $\Theta(\cdot)$.
Output: Synthesised dataset $\mathcal{D}_{aug}$.
Procedure
1) EWT
- Apply EWT to $x(t)$ to obtain $x_{EWT}(t)$

2) *Time-Delay Embedding*
- Form the state space:

$X(t) = [x_{\text{EWT}}(t), x_{\text{EWT}}(t-\tau), \cdots, x_{\text{EWT}}(t-(m-1)\tau)]$.

3) SINDy
- Identify a sparse set of governing equations by fitting:

$\dot{X}(t) = \Theta(X(t))\Xi$.

4) Synthetic Trajectories
- Perturb the initial conditions X_0 by ΔX_0.
- Numerically integrate the resulting ODEs to produce $X_{\text{synth}}(t)$.

5) Dataset Augmentation
- Concatenate $X_{\text{synth}}(t)$ with $X(t)$ to form the augmented dataset $\mathcal{D}_{aug}$.

Algorithm 1. EWT-SINDy for rotor fault diagnosis data augmentation.

4 Case study

To assess the efficacy of the proposed data augmentation method, termed EWT-SINDy, two datasets were employed. These consist of an experimental dataset and a simulated rotor system, both of which are detailed in the subsequent sections.

4.1 Experimental dataset: three-phase induction motor

This dataset was produced by assessing a 1 hp, 220V/380 V three-phase induction motor with a nominal speed and torque equal to 1715 rpm and 4.1 N m, respectively. The rotor, of squirrel cage type, was manipulated to simulate faults by introducing 1 to 4 adjacent broken bars (among a total of 34 bars); the broken bars were created through the drilling process. The experimental setup involved connecting the induction motor to a direct current generator via a shaft and employing a rotary torque wrench to measure the applied torque. This arrangement allowed for an effective control over mechanical loads, varying from 12.5% to 100% of the motor's full capacity, to simulate different operational stresses.

Data acquisition was performed utilising Vibrocontrol uniaxial vibration velocity sensors (model PU 2001) with a sensitivity of 10 mV/mm/s and a frequency range of 5–2000 Hz, capturing mechanical dynamics at multiple points around the motor, including tangential, axial, and radial measurements at both the drive and non-drive ends. Furthermore, electrical signals, i.e., three-phase voltages and currents were recorded using Yokogawa 96,033 current probes and oscilloscope voltage points directly from the motor's terminals. Under each specific working and health scenario, the test was replicated 10 times to ensure data consistency, with all measurements sampled at 8.327 kHz over 18 s, covering the motor's transition from transient to steady-state operations. Figure 2 represents the test rig of this dataset.

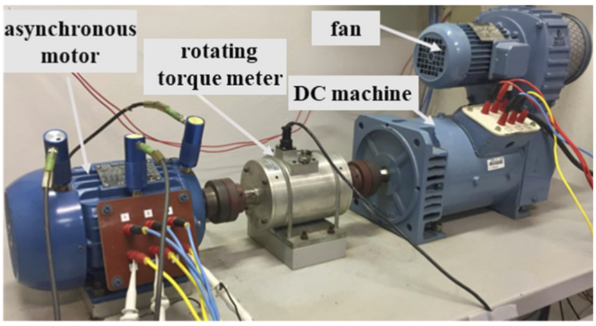

FIGURE 2
Workbench of the broken rotor bar dataset.

4.2 Numerical dataset: rotor-bearing-disc system

To generate the numerical dataset, a rotor system was modelled in MATLAB® R2024a by incorporating its equation of motion and embedding various faults. The FE model comprises a disc, coupling, bearing supports, dual shafts, and an electric motor, as displayed graphically in Figure 3. Within the FE platform, each component is depicted by a two-node element, where each node exhibits 4 degrees of freedom, i.e., rotational movements about the X and Y-axes and translational movements along these axes. The model specifies the lengths of the smaller shaft and the coupling as the lengths of each element, whilst the motor is represented as an alternating torsional torque at node 7. To simulate various states of system health, e.g., normal operation, an unbalanced disc, and parallel misaligned shaft conditions, modifications were made to the right-hand side ($f(t)$) of Equation 14, while other parameters remained unchanged.

$$M\{\ddot{q}\} + C\{\dot{q}\} + K\{q\} = f(t) \tag{14}$$

in which M, C, and K are the mass, damping, and stiffness matrices, in order. For the normal, unbalanced disc, and the misaligned rotor systems, $f(t)$ can be expressed as the Equations 15a–15c; respectively; Figure 4 shows the coordinate system for the left and right-hand sides of the node contains the coupling when suffering parallel misalignment.

$$\text{Normal } f(t) = f_m(t) = \frac{T_q}{r_m} cos(\omega_m t - \varphi_m) \tag{15a}$$

$$\text{Unbalanced} \begin{array}{ll} f(t) = f_m(t) + f_u(t) & F_X = m_d e\omega^2 cos(\omega t - \varphi_u) \\ f_u(t) = [F_X \; F_Y \; 0 \; 0] & F_Y = m_d e\omega^2 sin(\omega t - \varphi_u) \end{array} \tag{15b}$$

$$\text{Misaligned} \begin{array}{ll} f_1(t) = f_m(t) + f_{M1}(t) & f_2(t) = f_m(t) + f_{M2}(t) \\ f_{M1}(t) = [FX_1 \; FY_1 \; 0 \; 0] & f_{M2}(t) = [FX_2 \; FY_2 \; 0 \; 0] \\ MX_1 = T_q \, sin\,\theta_1 + K_b \varnothing_1 & MX_2 = T_q \, sin\,\theta_2 - K_b \varnothing_2 \\ MY_1 = T_q \, sin\,\varnothing_1 - K_b \theta_1 & MY_2 = T_q \, sin\,\varnothing_2 + K_b \theta_2 \\ FX_1 = \dfrac{(-MY_1 - MY_2)}{Z_3} & FX_2 = -FX_1 \\ FY_1 = \dfrac{(MX_1 + MX_2)}{Z_3} & FY_2 = FY_1 \\ \theta_1 = sin^{-1}\left(\dfrac{\Delta X_1}{Z_3}\right) & \theta_2 = sin^{-1}\left(\dfrac{\Delta X_2}{Z_3}\right) \\ \varnothing_1 = sin^{-1}\left(\dfrac{\Delta Y_1}{Z_3}\right) & \varnothing_2 = sin^{-1}\left(\dfrac{\Delta Y_2}{Z_3}\right) \end{array} \tag{15c}$$

The involving parameters in the above equations are listed in Table 2.

After modelling the discrepant health as well as operational scenarios, the resulting equations were solved through Houbolt time marching method with a time step of 2/2048 to record the vibration displacements at the different node locations. The results of this FE model are consistent with the modelled system through Abaqus/CAE model (Rezazadeh et al., 2023).

5 Results

To assess the effectiveness of EWT-SINDy in data augmentation and the subsequent fault diagnosis phase of rotary systems, the two aforementioned case studies were considered individually. The efficiency of the proposed framework was evaluated based on the intermediate results and the accuracy of fault diagnosis in these two systems. It is important to note that the additional state of variables generated through the time delay embedding phase was solely used to aid in identifying the systems' dynamics. During the training and testing phases of fault detection, only the EWT coefficients of the original state variables were fed into the damage identification structure.

5.1 Broken rotor bar system

In this case study, four load conditions were applied with torsional torques of 1, 2, 3, and 4 N m. Under each load condition, 5 health scenarios were examined: normal, and rotor with 1, 2, 3, and 4 broken bars. From 10 observations available per health scenario at each load, one was selected for analysis and data generation through EWT-SINDy, whilst the remaining nine observations were assigned to the test phase. Synthetic signals were used exclusively for training; all reported test accuracies were obtained on real sensor measurements never used in identification or augmentation stages.

The selected signals were first detrended and subsequently decomposed using EWT up to level 2, selecting only signals from this level for further processing; numerical derivatives were calculated using a fourth-order central difference method.

For the SINDy algorithm, a library of first-order polynomial terms $\{1, x_i\}$ was employed. Trigonometric functions $\{\sin(x_i), \cos(x_i)\}$ were evaluated during preliminary calibration on a subset of training data (normal condition, T = 2 N m): their inclusion resulted in zero-valued coefficients for all trigonometric terms after sparse regression at $\lambda \geq 0.1$, increased the candidate library dimension by 40%, and produced no

 10.3389/fmech.2026.1810068

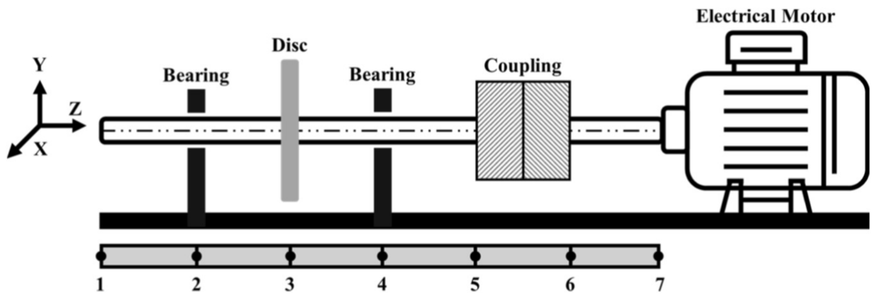

FIGURE 3
Diagram illustrating the rotor-bearing-disc assembly with coupling, accompanied by the FE model of the system.

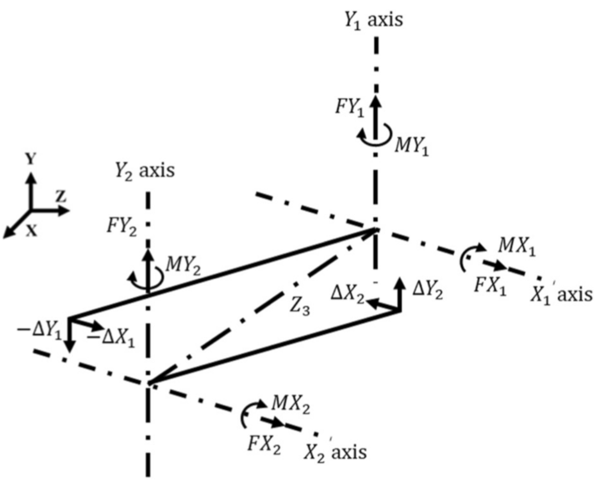

FIGURE 4
Coordinate system for coupling under conditions of parallel misalignment.

measurable reduction in reconstruction RMSE (< 0.5% change). Second-order polynomial terms $\left\{1, x_i, x_i x_j, x_i^2\right\}$ were similarly assessed: their inclusion expanded the candidate set from 11 to 66 functions for the 10-dimensional embedded state without improving reconstruction beyond the noise floor, whilst increasing computational cost. First-order polynomials without trigonometric terms were therefore retained for parsimony and interpretability.

A time delay embedding was applied with a dimension (m) of 2 and a delay (τ) of 1 to increase the system dimension from 5 to 10. A grid search was performed to optimise the sparsity factor (λ), ranging from 0.001 to 2, divided into 50 equal intervals. The optimal λ was determined based on the minimum root mean square error (RMSE) between the original and reconstructed signals.

The sparsity parameter λ was selected through a two-stage process to avoid overfitting. For each operating condition, the single real observation was split into training (first 70% of time series) and validation (remaining 30%) segments. The grid search over $\lambda \in [0.001, 2]$ evaluated reconstruction RMSE on the validation segment, with the optimal value selected as that minimising validation error. This procedure was repeated independently for each health condition and operating point, causing condition-specific λ values typically ranging between 0.3 and 0.8. The test set, comprising 9 independent observations per condition, remained entirely unseen during both λ selection and synthetic data generation.

The identified system of ODEs was solved numerically using the ODE45 solver, starting from perturbed initial conditions derived from the first data points of the original state variables, adjusted randomly by 0.1%. This process was repeated 149 times to produce a dataset, which was then merged with the original seed observation employed as framework input to form a total of 150 observations for each health and operating condition. Except for λ (selected by RMSE minimisation), all other settings including the numerical derivative

TABLE 2 **Key mechanical and dynamical parameters of the rotor system.**

Symbol	Description	Symbol	Description
f_u	Unbalanced force	ω_m	Motor angular velocity
f_{M1}	Left-hand side nodal misalignment force	φ_m	Phase angle of the motor
f_{M2}	Right-hand side nodal misalignment force	m_d	Mass of the disc
T_q	External torsional torque	e	Eccentricity of the disc
r_m	Radius of the shaft of the motor	ω	Angular velocity of the rotor
K_b	Flexure coupling bending spring rate per diaphragm	φ_u	Phase angle of the unbalancing force
ΔY	Misalignment severity in Y-direction	ΔX	Misalignment severity in X-direction

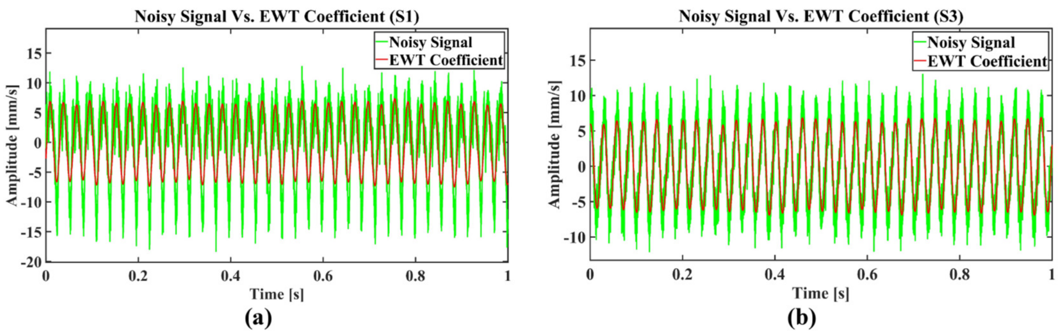

FIGURE 5
Noisy signals versus EWT coefficients of **(a)** radial vibration speed on the driven side and **(b)** radial vibration speed on the non-driven side.

scheme were established through preliminary empirical calibration and kept constant across runs.

To better simulate real-world applications and evaluate the EWT-SINDy framework's capability in handling noisy conditions, additive white Gaussian noise (AWGN) at a signal-to-noise ratio (SNR) of 10 dB was introduced to the captured signals. This noise level represents realistic industrial operating conditions commonly encountered in rotating machinery fault diagnosis. Figures 5a,b illustrate the noise-augmented versions of the original signals and their subsequent detrending and decomposition via the EWT process under normal conditions, when a torsional torque of 1 N m was applied to the rotor system. These figures display only 1 s of the signals from sensors measuring radial vibration speed on the driven (S1) and the non-driven sides (S3), respectively, equivalent to 9,000 data points, for enhanced visual clarity.

Figure 5 shows that the EWT process reduced noise and extracted dominant dynamic components for the tested condition. In particular, the EWT decomposition isolated the fundamental and low-order harmonics of the rotor's vibration response whilst attenuating higher-frequency noise, so enhancing signal clarity. This behaviour illustrates the intended role of EWT within the framework, namely, to provide smoother, noise-reduced coefficient trajectories on which SINDy can identify stable dynamics.

Given that the delay factor (τ) was set to a low value, i.e., 1, the distinctions between the original and embedded dimensions of the EWT coefficients of a state variable are not readily apparent in the time-domain graph. Nevertheless, these subtle differences have the potential to enhance the capability to unravel the dynamics using EWT-SINDy. Figures 6a,b depict scenarios where the embedding stage was deactivated and activated for reconstructing EWT coefficients, respectively.

The differences between the extracted and the reconstructed EWT coefficients in Figure 6a show that without employing embedding, the framework cannot capture the true dynamics of the system. Conversely, Figure 6b illustrates the enhanced clarity in the signal's behaviour when embedding is activated, thereby improving the EWT-SINDy method's effectiveness in elucidating the underlying dynamical structures. Thus, the delay embedding is not only a technical step but a necessary condition for recovering dynamics that are consistent with the observed evolution of the EWT coefficients.

If no sparsity thresholding is applied, each ODE describing a signal consists of 11 terms, with 10 corresponding to the state variables (after delay embedding) and one constant term. The sparsity factor (λ) plays a crucial role in determining the accuracy of system identification in the SINDy method, necessitating a balance between accuracy and interpretability (sparsity). Equation 16 presents the complete general form of the ODEs for the broken rotor bar system with an embedded dimension of 10.

$$\frac{dX_i}{dt} = c_{1i} + \sum_{j=1}^{10} C_{ij+1} X_j, \text{for } i = 1, \cdots, 10 \tag{16}$$

in which C_{ij+1} represents the coefficients corresponding to each X_j. The introduction of a non-zero sparsity factor reduces the quantity of active terms within the ODEs. For instance, in the coefficient matrix C_{ij} associated with an observation from the scenario of the rotor suffering 4 broken bars under the loading condition of T = 1 N m, all array elements remain active when $\lambda = 0$. In contrast, when $\lambda = 0.5$, the number of active arrays is reduced to 76 from 110; here C_{ij} indeed is Ξ that is the matrix includes the coefficients in a sparse format. Figure 7 visually illustrates the active terms in the C_{ij} for $\lambda = 0$ and Ξ for $\lambda = 0.5$ for the above-mentioned observation belonging to r4b class.

After adjusting the initial conditions and solving the system of ODEs using the Dormand-Prince method, which is a Runge-Kutta (4,5) pair, the EWT-SINDy pipeline generated 149 synthetic samples (comprising EWT coefficients) for each health scenario (class). These samples, along with one original observational data point per class, were used to train and validate the fault diagnosis model. For testing, the model was evaluated on 9 independent sensor-recorded observations from the experimental test rig, ensuring no overlap with the training/validation data. The distribution of observations across the training, validation, and testing phases is depicted in Figure 8. In the following sections of this work and for this specific case study, the healthy condition, 1 broken rotor bar, 2 broken rotor bars, 3 broken rotor bars, and 4 broken rotor bars are denoted as classes 'rs', 'r1b', 'r2b', 'r3b', and 'r4b', respectively.

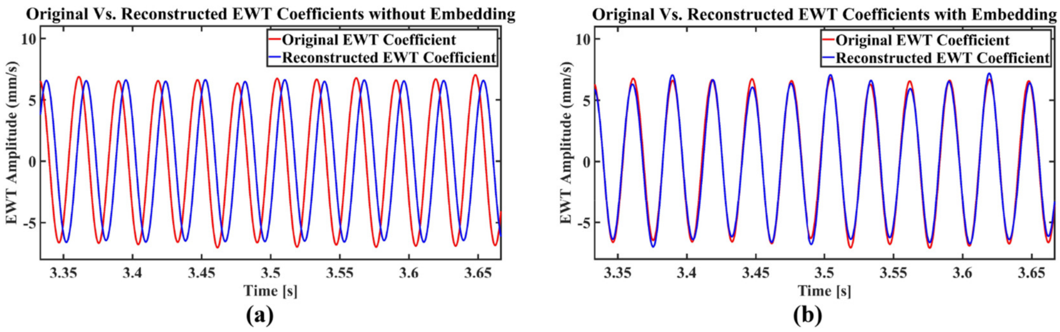

FIGURE 6
Comparison of original and reconstructed EWT coefficients through EWT-SINDy: **(a)** without time delay embedding and **(b)** with time delay embedding implemented.

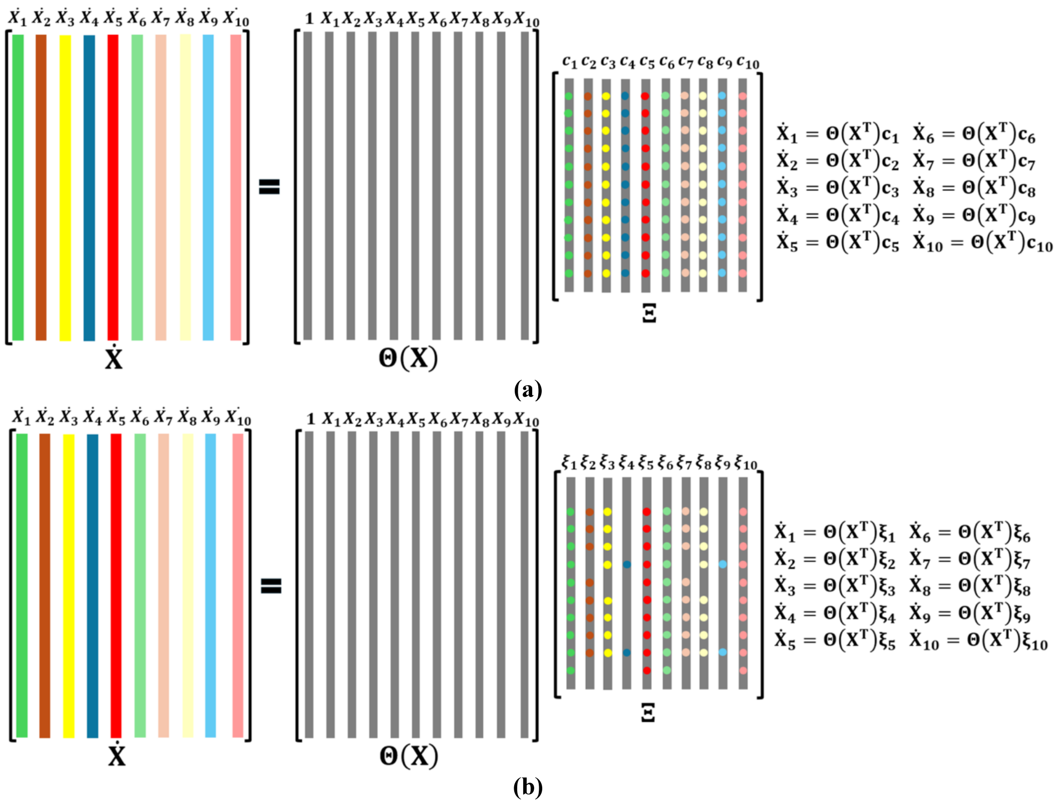

FIGURE 7
Graphical visualisation of active terms in the **(a)** coefficient matrix C_{ij} (λ = 0) and **(b)** sparse matrix Ξ (λ = 0.5) for the r4b rotor system under T = 1 N m loading.

To demonstrate the efficacy of the designed data augmentation framework in the fault diagnosis of rotor systems, a convolutional neural network (CNN) model was subsequently developed as the classification (fault detection) model. This network is recognised for its capacity to efficiently extract intricate fault characteristics from vibration data, while also ensuring swift computational performance (Qian et al., 2024; Zhao et al., 2024c). The number of layers and the size of the convolution layers can be adjusted based on the complexity of the signal. However, as one of the objectives of this work is to develop a framework suitable for real-time execution, a simple CNN model was employed, with its structure detailed in Table 3. It should be noted that both the input layer and the fully connected layer have a size of 5. The input layer is sized this way to accommodate signals from 5 channels (accelerometers), while the fully connected layer corresponds to the 5 classes of health scenarios.

In the training protocol, the maximum number of epochs was established at 20, with a mini-batch size of 32; the ADAM optimiser

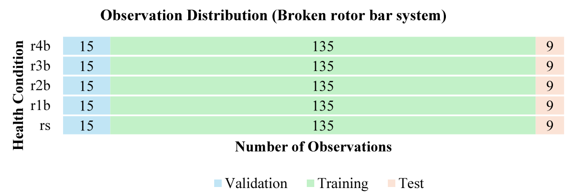

FIGURE 8
Observation counts in the fault diagnosis model phases of the broken rotor bar system.

was employed. Validation was scheduled to execute every 5 mini-batch iterations.

To depict the introduced variabilities in the generation of the training dataset and to evaluate the efficacy of the feature extraction layers within the proposed CNN architecture, Figure 9a presents the swarm scatter chart for the training set under the loading condition of T = 1 N m. Correspondingly, Figure 9b displays the swarm scatter chart for the test set under the same loading condition. Notably, the features utilised for these visualisations were derived from the outputs of layer 13 (the global average pooling layer); principal component analysis (PCA) was subsequently applied to these features to reduce their dimensionality prior to their representation in the swarm scatter chart.

The swarm scatter plots demonstrate evident clustering patterns among health scenarios in both the training dataset and the dimensionality-reduced PCA space, signifying that CNN's global average pooling layer successfully distinguishes between features. Within the test dataset, the spatial arrangement of distinct classes corresponds closely to the groupings observed in the training data, highlighting the model's ability to generalise the learned features effectively when exposed to equivalent operational conditions. Furthermore, the spread of discrepant observations in the distinct zone of each health scenario represents that adequate variability was introduced during the data generation phase of the training dataset.

The confusion matrices in Figures 10a–d display the fault diagnosis results of rotor systems on the assumption of employing 1, 2, 3, and 4 N m, in order.

The fault diagnosis results in Figure 10 demonstrate that the datasets generated using EWT-SINDy data augmentation effectively trained the classification framework. Under the highest torsional loading condition (T = 4 N m), only two out of 45 observations were misclassified. Analysis of these test observations revealed potential issues during testing, as all 9 observations from the r4b class were separately evaluated using EWT-SINDy. The results indicated that the two misclassified observations could not be accurately reconstructed through EWT-SINDy, due to experimental challenges such as sensor installation issues. Similar behaviour was observed in preliminary trials at slightly higher and lower SNR values, suggesting that the reconstruction and classification performance did not degrade abruptly around the chosen 10 dB level. Figure 11 displays the results of EWT coefficient reconstruction through the EWT-SINDy framework for 2 observations belonging to the T = 4 N m condition, assuming r4b. One of these observations (illustrated in Figure 11a) is the one that could not be reconstructed properly (observation number 9), while the observation plotted in Figure 11b was selected from the remaining 7 observations in the same class that were classified correctly (observation number 10). It should be emphasised that both Figures 11a–b represent the EWT of the radial vibration speed on the driven side.

In Figure 11a, the original EWT coefficients show a smooth pattern, while the reconstructed ones exhibit irregularities, particularly between 2 and 3 s, indicating reconstruction challenges for observation number 9. In contrast, Figure 11b demonstrates a close match between the original and reconstructed coefficients for observation number 10, reflecting accurate reconstruction and classification. This contrast

TABLE 3 CNN architecture for fault diagnosis.

No.	Layer	Key parameters	No.	Layer	Key parameters
1	Sequence input	Number of features: 5	9	Max pooling 1D	Pool size: 2 Stride: 2
2	1D convolution	Filter size: 3 Number of filters: 16 Padding: Same	10	1D convolution	Filter size: 3 Number of filters: 64 Padding: Same
3	Batch normalisation	Normalises activations and gradients, improving training stability	11	Batch normalisation	-
4	ReLU activation	Applies the rectified linear unit function	12	ReLU activation	-
5	Max pooling 1D	Pool size: 2 stride: 2	13	Global average pooling	Averages feature maps across the time dimension, reducing them to a single feature per map
6	1D convolution	Filter size: 3 Number of filters: 32 Padding: Same	14	Fully connected	Output size: 5 (corresponding to the 5 fault classes)
7	Batch normalisation	-	15	Softmax layer	Converts the outputs to probability distributions over the 5 classes
8	ReLU activation	-	16	Classification layer	Assigns final class labels based on highest probability

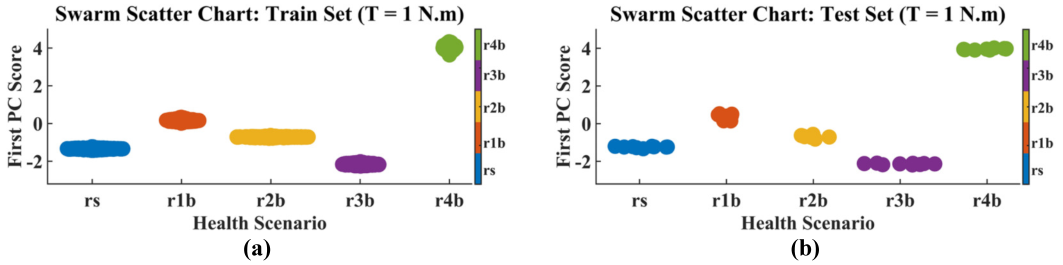

FIGURE 9
Swarm scatter chart for the broken rotor bar system under loading of T = 1 N m for **(a)** the training dataset and **(b)** the testing dataset.

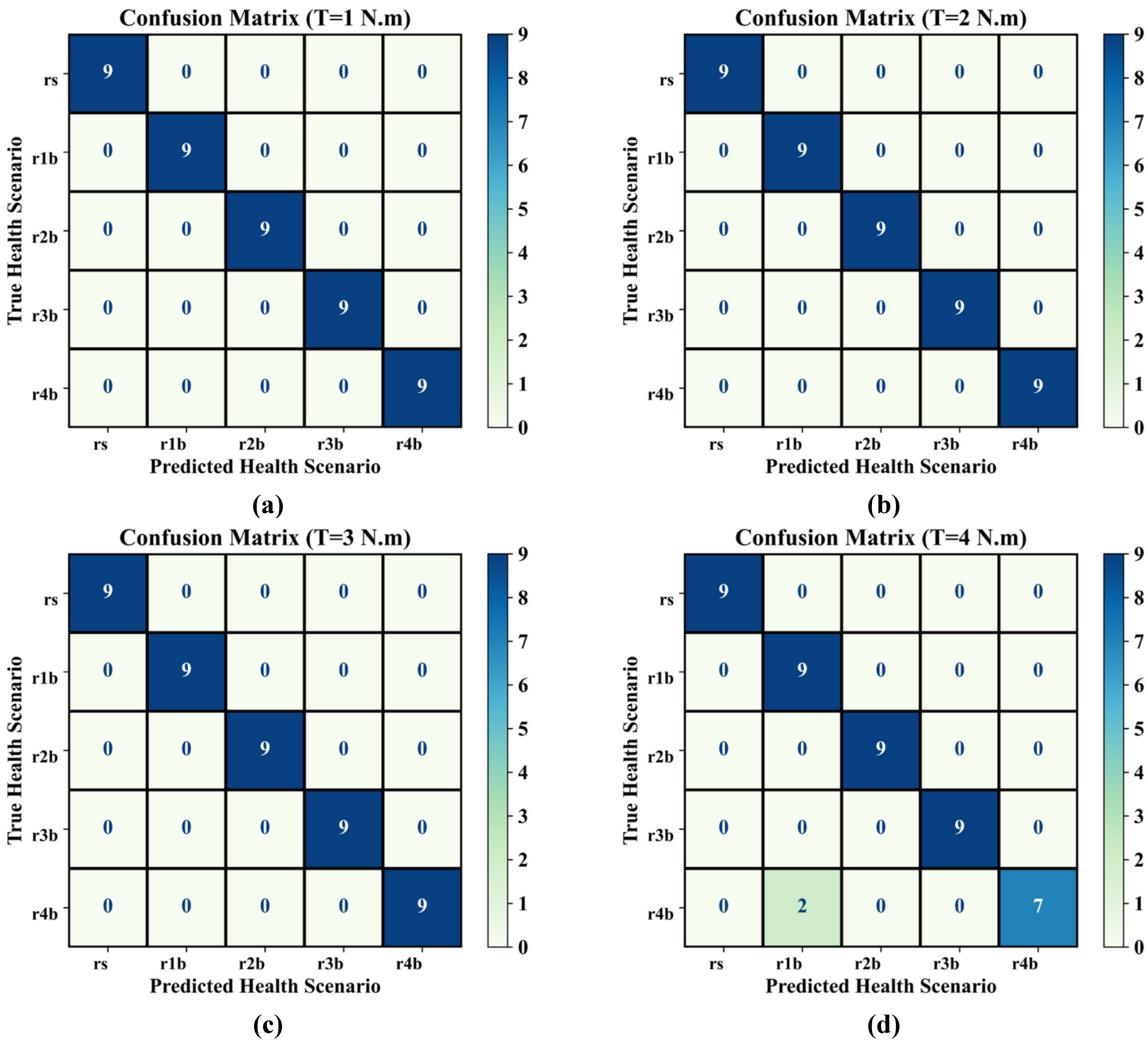

FIGURE 10
Confusion matrices for fault diagnosis under different loading conditions for broken rotor bar system: **(a)** 1 N m, **(b)** 2 N m, **(c)** 3 N m, and **(d)** 4 N m.

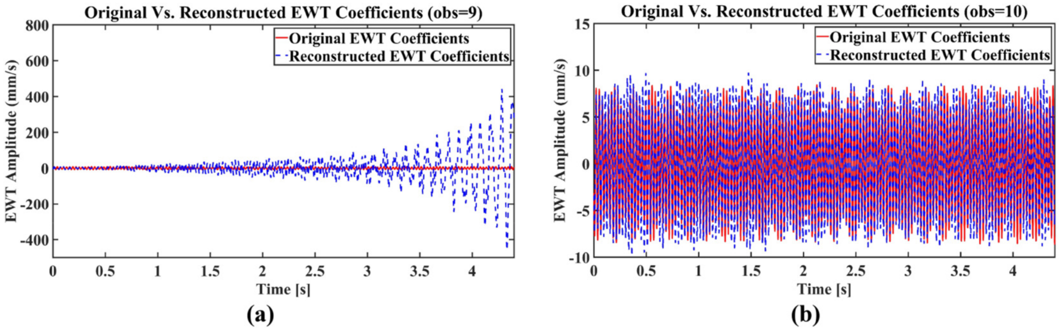

FIGURE 11
Original versus reconstructed EWT coefficients for **(a)** a misclassified observation (obs = 9) and **(b)** a correctly classified observation (obs = 10).

underscores the sensitivity of the EWT-SINDy framework to experimental variabilities such as inconsistent sensor mounting, transient mechanical disturbances, and fluctuating background noise that can be considered as factors that can distort signal dynamics and degrade system identification accuracy. In practice, this mismatch between original and reconstructed EWT coefficients provides a physically grounded warning signal that the underlying measurement configuration is unreliable, which is information that conventional purely data-driven augmentation models do not expose.

To mitigate these effects, the framework was extended to incorporate multiple real observations per health condition. To this end, 3 observations from each class were reassigned for data synthesis, reducing the test set from 9 to 7 observations per class. Each of the 3 seed observations was processed independently through EWT-SINDy to extract a distinct set of governing equations, and 69 synthetic trajectories were generated from each seed by perturbing its initial conditions. Together with the 3 original seed observations, this led to $3 + (3 \times 69) = 210$ trajectories per class in total, of which 189 were allocated to the training set and 21 (including the 3 original seeds and 18 synthetic trajectories) to the validation set, consistent with the 10% validation split used in the single-seed configuration. This approach enhances robustness by capturing intra-class variability and reduces reliance on any single observation. Figures 12, 13 present the updated observation allocation across the diagnosis phases and the confusion matrices for fault classification under all loading conditions, respectively, in the enhanced configuration.

The fault diagnosis results shown in the confusion matrices of Figure 13 indicate that increasing the number of real observations assigned to the EWT-SINDy framework, along with synthesising data from these inputs, led to improved classification accuracy under the previously challenging condition of T = 4 N m. Meanwhile, the accuracy for the other loading conditions remained consistent with earlier results, maintaining a perfect classification rate of 100%.

5.2 Rotor-bearing-disc system

To evaluate the effectiveness of EWT-SINDy in diagnosing faults in a rotor-bearing-disc system, two angular velocities (85 rad/s and 115 rad/s) were analysed. For each of the 3 health conditions (healthy, unbalanced disc, and misaligned rotor), one observation was generated using the detailed MATLAB® R2024a FE simulation in the previous sections. Initial conditions were then perturbed to produce 149 additional observations per condition, which were combined with the simulated observation to create datasets of 150 observations per condition at each speed. These augmented datasets were used solely for training the fault diagnosis models, while test performance was assessed on independently simulated responses that were excluded from both the identification and augmentation stages. The methodology previously implemented for the broken rotor bar case was likewise employed in this case study to identify the optimal λ value, resulting in 0.2 and 0.6 as the most effective parameters.

System dynamics were captured by measuring displacement vibrations at two bearing housings in 4 directions (translational and rotational along X and Y-axes), resulting in 8 state variables; throughout the time delay embedding process the dimension of the system was enhanced to 16 with a delay factor of 1. The EWT coefficients at level 2 were chosen for the further steps. Table 4 denotes the mechanical parameters used for the modelling and simulating the rotor-bearing-disc system.

During the testing phase for angular velocities of 85 rad/s and 115 rad/s, 20 observations were generated for each of the 3 system conditions: normal (Norm), unbalanced (Unb), and misaligned (Mis), using the FE model. To introduce variability within the same class, the magnitude of multiple mechanical parameters, such as eccentricity, motor phase angle, and initial conditions, were altered for a specific observation. Furthermore, AWGN at a SNR of 10 dB was incorporated into the simulated signals to replicate real-world industrial conditions and ensure fair comparison with the experimental broken rotor bar dataset. Figure 14 reveals the distribution of the observations for the 3 phases of the fault diagnosis; it is worthwhile to mention that the same distribution was implemented for both operating conditions.

To illustrate the influence of applying EWT in analysing the dynamics of the rotor-bearing-disc system, SINDy-based signal reconstruction was conducted on both the unprocessed noisy signal and the filtered signal (through the EWT), corresponding to the transverse Y-direction vibration displacement, under misaligned conditions (simulated at a rotational velocity of 85 rad/s). The results are presented in Figures 15a–b, respectively.

Comparing the reconstruction results in Figure 15, it is evident that the SINDy method struggles to accurately identify the dynamics of the rotor-bearing-disc system when applied directly to the

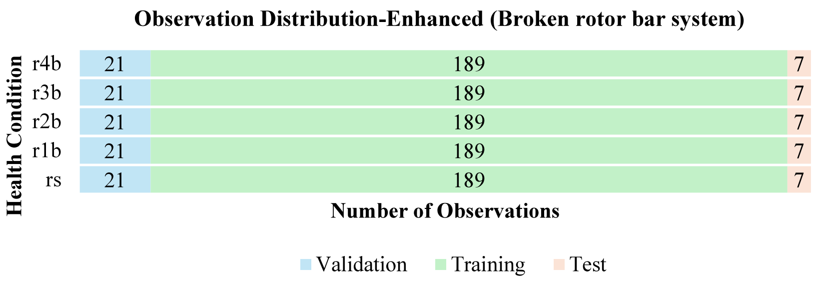

FIGURE 12
Observation allocation across training, validation, and testing phases for the broken rotor bar system under the enhanced multi-observation configuration.

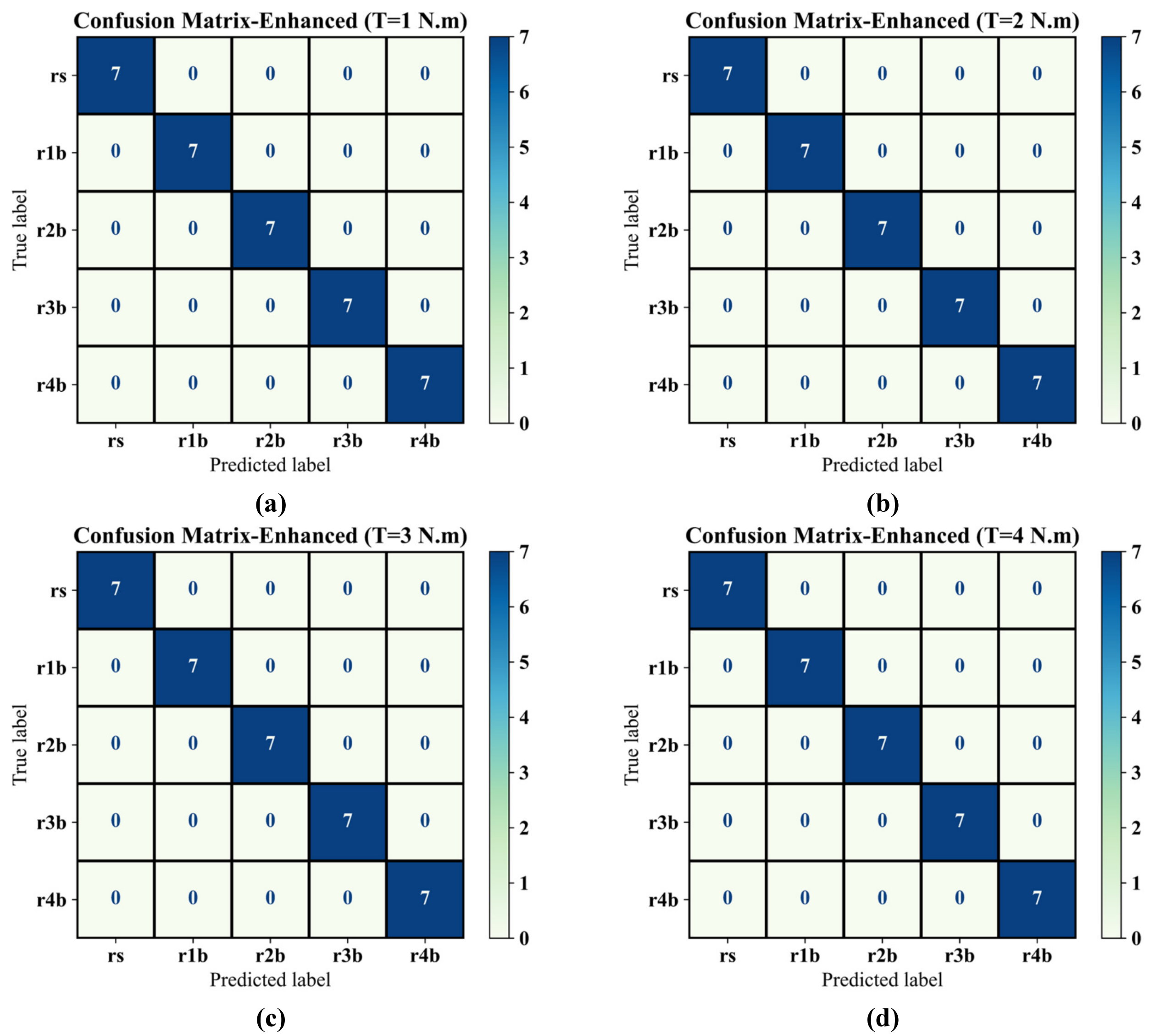

FIGURE 13
Confusion matrices for fault diagnosis under different loading conditions using the enhanced training dataset for broken rotor bar system: **(a)** 1 N m, **(b)** 2 N m, **(c)** 3 N m, and **(d)** 4 N m.

TABLE 4 Mechanical properties of the rotor-bearing-disc system.

Parameter	Value	Parameter	Value
Disc mass	2 kg	Shaft length	10 cm
Eccentricity	5 mm	Polar moment of inertia	$6.25 * 10^{-4}$ kg·m^2
Motor phase angle	0 rad	Bearing stiffness	$5 * 10^7$ N/m
Misalignment phase angle	45 rad	Damping coefficient	350 N s/m
Shaft material density	7,800 kg/m^3	Motor force amplitude	150 N
Driven shaft diameter	50 mm	Driver shaft diameter	38 mm
Shaft Young's modulus	$2.08 * 10^{11}$ Pa	AC motor frequency	50 Hz

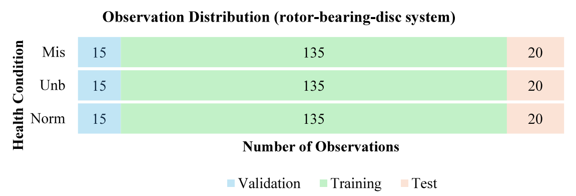

FIGURE 14
Observation counts in the fault diagnosis model phases of the rotor-bearing-disc system.

unprocessed noisy signal, as shown in Figure 15a. In contrast, Figure 15b demonstrates that pre-processing the signal with EWT significantly enhances the reconstruction quality. The filtered EWT coefficients enable SINDy to isolate the system's essential dynamics, resulting in a high-precision alignment between the original and reconstructed coefficients. The contrast between panels (a) and (b) shows that, for the simulated rotor-bearing-disc system, SINDy becomes a dependable dynamical model only once the signal has been filtered through EWT.

To train the fault diagnosis model, the same CNN structure outlined in Table 3 was used, although the sizes of the input layer and the fully connected layer were adjusted to 8 (representing the number of original state variables) and 3 (corresponding to the number of health scenarios), respectively. Graphs in Figures 16a–b present the swarm scatter plots for the training and testing phases of the observations simulated and generated at $\omega = 85$ rad/s. Similar to the previous case study, the dimensionality of the outputs from layer 13 was reduced, and the corresponding swarm scatter plots were subsequently plotted.

The swarm scatter plots in Figure 16 demonstrate the effectiveness of the EWT-SINDy method for feature extraction and dataset augmentation. Clear separation between the normal, unbalanced, and misaligned rotor-bearing-disc systems in both training (a) and testing (b) sets underscores the method's ability to capture discriminative features intrinsic to each operational state. The controlled variabilities introduced through augmentation are evident in the distinct cluster formations, with minimal overlap, ensuring a robust representation of class-specific dynamics.

After the training, validation, and testing phases of the model, the results were displayed in the confusion matrices in Figures 17a–b, corresponding to angular speeds of 85 rad/s and 115 rad/s.

The fault diagnosis results, derived from numerically simulated test datasets, demonstrate high accuracy: 98.3% at 85 rad/s (1 normal instance misclassified as unbalanced) and 100% at 115 rad/s. The single misclassification at 85 rad/s may stem from simulation-induced feature overlaps between normal and unbalanced conditions, reducing separability. Perfect accuracy at 115 rad/s suggests enhanced discriminative features under higher angular velocities, reflecting the model's robustness to operational variations. Complementary simulations at slightly higher and lower SNR values generated comparable reconstruction and classification performance, indicating that the observed accuracy is not overly sensitive to the exact choice of the 10 dB noise level.

Similar to the preceding case study, for the simulated rotor-bearing-disc system, the size of the training set was further increased by allocating additional observations to the EWT-SINDy data-synthesis framework, in order to further analyse the impact of operational and noise variabilities on fault diagnosis. To carry out this, 2 additional observations per class were processed through EWT-SINDy alongside the original seed, resulting in three independent sets of governing equations. From each set, 69 synthetic trajectories were generated by perturbing initial conditions, producing $3 + (3 \times 69) = 210$ trajectories per class in total. Of these, 189 were allocated to training and 21 to validation (Figure 18). The test set remained unchanged at 20 independently simulated observations per class. Figure 18 reveals the enhanced data distribution; Figure 19 represents the results of the fault diagnosis in terms of the confusion matrices for the two various angular velocities.

As shown in Figure 19, this augmentation improved model generalisability, with fault diagnosis achieving 100% accuracy across both rotational speeds of 85 rad/s and 115 rad/s. By incorporating multiple simulated observations per class into the synthesis process, the approach mitigates overfitting risks and ensures that dynamic variability is adequately captured, thereby addressing potential concerns regarding the robustness and data dependency of the EWT-SINDy framework.

5.3 Comparative study

Whilst the primary strength of the EWT-SINDy framework lies in generating interpretable, physics-guided synthetic data, its

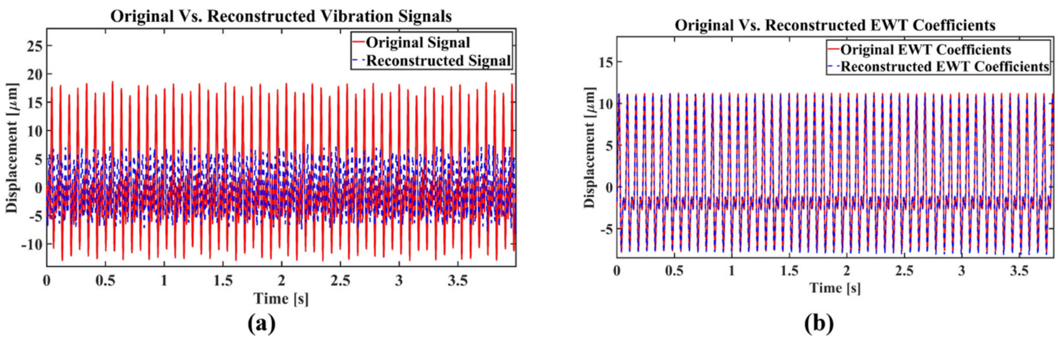

FIGURE 15
Y-direction vibration displacement signals under misaligned conditions (85 rad/s): **(a)** raw unprocessed signal (without applying EWT) and **(b)** EWT-SINDy reconstructed signal.

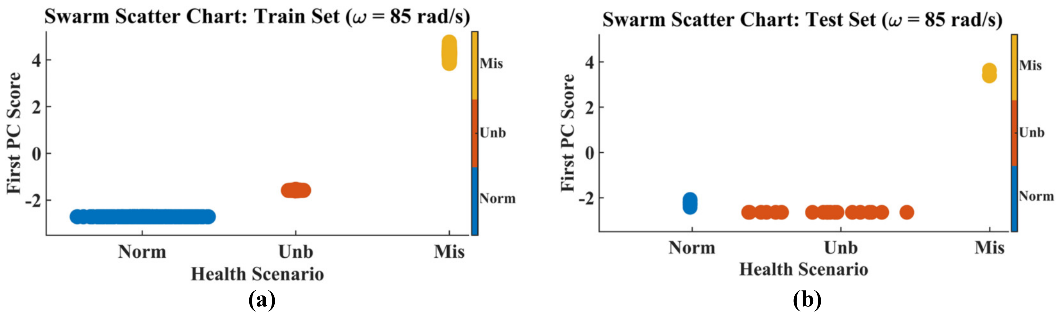

FIGURE 16
Swarm scatter chart for the rotor-bearing-disc system with angular velocity of ω = 85 rad/s for **(a)** the training dataset and **(b)** the testing dataset.

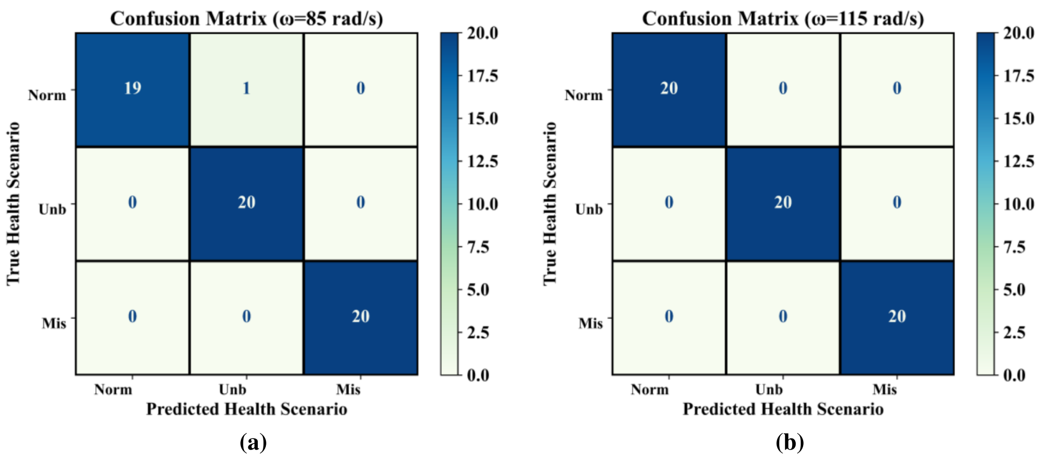

FIGURE 17
Confusion matrices for fault diagnosis under different rotational velocities for rotor-bearing-disc system: **(a)** 85 rad/s and **(b)** 115 rad/s.

performance was benchmarked against four established data augmentation methods designed for few-shot scenarios: mixup-based data augmentation (Mixup-DA) (Yu et al., 2025), auxiliary classifier generative adversarial network (ACGAN) (Shao et al., 2019), variational autoencoder (VAE) (Kingma and Welling, 2019), and a standard generative adversarial network (GAN) (Goodfellow et al., 2020). To ensure fair comparison, all methods were trained to generate 149 synthetic samples per class from one or three real observations, matching the EWT-SINDy setup, and were evaluated on identical test sets comprising real sensor

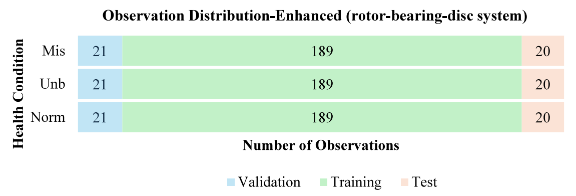

FIGURE 18
Observation counts in the fault diagnosis model phases of the rotor-bearing-disc system under the enhanced multi-observation configuration.

measurements. The same CNN architecture described in Table 3 was used for feature extraction and classification across all approaches. Key hyperparameters for each method were optimised via grid search on the validation set, whilst other architectural parameters followed established practices in the literature. Table 5 presents the hyperparameter configurations for all 4 baseline methods.

5.3.1 Mixup-DA performance

The damage classification outputs for the two data availability scenarios are represented in bar charts of Figures 20a–b for the broken rotor bar and rotor-bearing-disc systems, respectively, using Mixup-DA augmentation.

Figure 20 demonstrates that using only a single observation for data synthesis with Mixup-DA resulted in significantly lower accuracy compared to the EWT-SINDy framework. This is attributed to insufficient variability captured in the training data, which limits Mixup-DA's ability to generalise under extreme data scarcity. Increasing the number of observations to 3 improved the quality of the generated datasets during the training phase in both case studies. However, even with this enhancement, the accuracy remained at least 17% lower than that achieved using the EWT-SINDy framework under identical conditions.

5.3.2 ACGAN performance

The results of damage classification for the two data availability scenarios are presented as bar charts in Figure 21a for the broken rotor bar system and in Figure 21b for the rotor-bearing-disc system, using ACGAN augmentation.

A comparison of the results shown in Figure 21 with those obtained from EWT-SINDy and Mixup-DA indicates that the ACGAN approach caused the lowest performance among all three methods. This difference is particularly pronounced in the scenario where only a single observation was available for data synthesis. Under these conditions, the highest classification accuracy achieved for the broken rotor bar system did not exceed 34% (at T = 3 N m), whilst the performance for the rotor-bearing-disc system was even lower, with a maximum accuracy of 28% (at ω = 115 rad/s). Although the use of an augmented dataset (3 observations) led to improved accuracy in both case studies, the results remained below those attained by both the EWT-SINDy and Mixup-DA methods.

5.3.3 VAE performance

The damage classification results for both data availability scenarios are presented in Figure 22, with panel (a) corresponding to the broken rotor bar system and panel (b) to the rotor-bearing-disc system, using VAE-based augmentation.

Figure 22 demonstrates that the VAE-based augmentation achieved moderate classification accuracy when using 3 seed observations, reaching up to 83% for the broken rotor bar system at T = 2 and T = 3 N m, and up to 72% for the rotor-bearing-disc system at 115 rad/s. However, the single-seed scenario produced lower accuracy in both case studies, indicating that the VAE struggled to learn a meaningful latent distribution from a single observation. Even with 3 seed observations, the accuracy remained at least 17% below that of the EWT-SINDy framework across all conditions, with the most pronounced gap observed in the rotor-bearing-disc system where the highest VAE accuracy (72%) fell 28 percentage points below the proposed method. These results

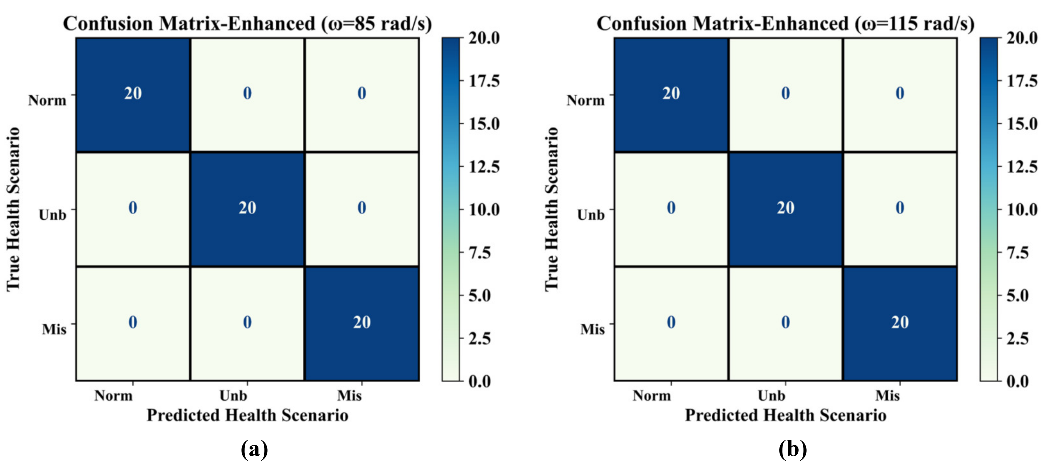

FIGURE 19
Confusion matrices for fault diagnosis under different rotational velocities using the enhanced training dataset for rotor-bearing-disc system: **(a)** 85 rad/s and **(b)** 115 rad/s.

TABLE 5 Hyperparameter values for the four baseline augmentation methods.

Parameter	Mixup-DA	ACGAN	VAE	GAN
Latent dimension	n.a	50	20	20
Learning rate	0.001	0.0001	0.0001	0.0001
Interpolation coefficient	0.2	n.a	n.a	n.a
Batch size	n.a	1, 3	1, 3	1, 3
Number of epochs	n.a	1,500	1,500	1,500
Optimiser	n.a	Adam	Adam	Adam
Activation function	n.a	ReLU	ReLU	ReLU
Gradient clipping	n.a	n.a	1.0	n.a
Weight decay	n.a	n.a	0.00001	n.a
Loss function	n.a	Binary cross-entropy	KL divergence + reconstruction	Binary cross-entropy

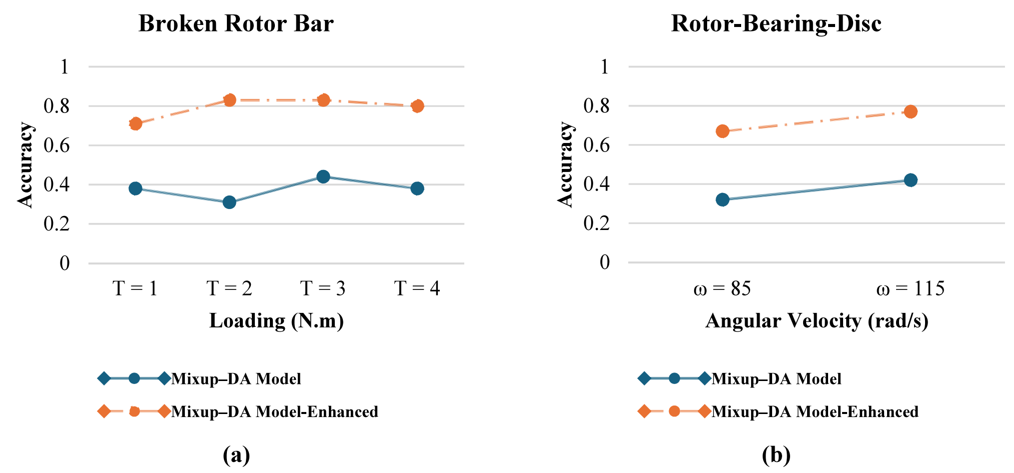

FIGURE 20
Fault diagnosis results utilising Mixup-DA data augmentation for **(a)** broken rotor bar and **(b)** rotor-bearing-disc systems.

suggest that, under extreme data scarcity, the VAE's reliance on learning a continuous latent space is constrained by the limited diversity of the available training samples.

5.3.4 GAN performance

The damage classification results for both data availability scenarios are presented in Figure 23, with panel (a) corresponding to the broken rotor bar system and panel (b) to the rotor-bearing-disc system, using GAN-based augmentation.

Figure 23 shows that the standard GAN produced mixed results across the two case studies. For the broken rotor bar system, the single-seed configuration achieved accuracy between 34% and 46%, while the enhanced configuration with 3 seed observations improved accuracy to between 62% and 69%. Despite this improvement, the GAN remained at least 31 percentage points below the EWT-SINDy framework across all loading conditions. For the rotor-bearing-disc system, the GAN performed comparatively better, reaching 87% and 88% accuracy in the enhanced configuration at 85 and 115 rad/s, respectively. This disparity between the two case studies suggests that the GAN can capture simpler dynamical patterns (3 health classes with distinct fault signatures) more effectively than complex multi-class fault structures (5 health classes with incremental severity differences). Nevertheless, the GAN remained below the proposed framework in all conditions, and its performance in the broken rotor bar system was notably lower than both the VAE and Mixup-DA baselines, reinforcing the advantage of physics-guided augmentation over purely generative approaches under data-scarce conditions.

5.3.5 Synthetic data quality and computational cost

To supplement classification accuracy, the distributional quality of the synthetic data produced by each method was assessed by estimating the maximum mean discrepancy (MMD) between the feature distributions of the real test set and the synthetic training set using a Gaussian radial basis function kernel. Prior to computing

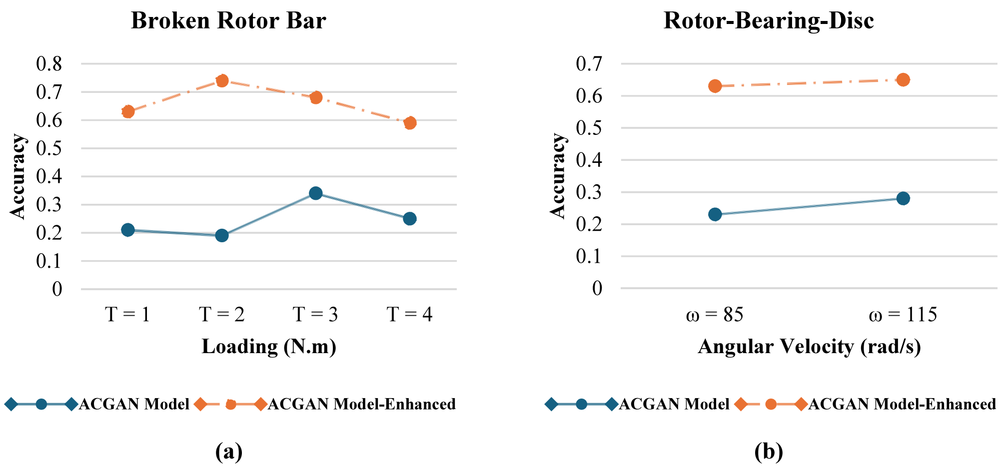

FIGURE 21
Fault diagnosis results utilising ACGAN data augmentation for **(a)** broken rotor bar and **(b)** rotor-bearing-disc systems.

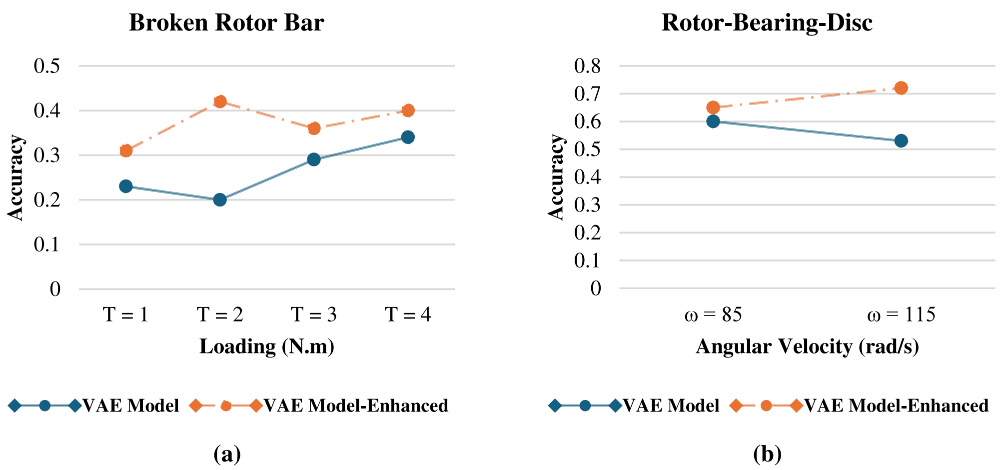

FIGURE 22
Fault diagnosis results utilising VAE data augmentation for **(a)** broken rotor bar and **(b)** rotor-bearing-disc systems.

MMD, all signals were normalised to the [0, 1] interval using the minimum and maximum values of each state variable from the original observations, ensuring scale-consistent comparison across methods and case studies. Lower MMD values indicate closer alignment between synthetic and real data distributions. Table 6 reports this metric alongside the data generation time per loading condition (broken rotor bar) and per angular velocity condition (rotor-bearing-disc) for each method.

As shown in Table 6, EWT-SINDy achieved the lowest MMD across both case studies, indicating the closest distributional alignment between synthetic and real data. Among the baseline methods, GAN and ACGAN produced lower MMD values than VAE and Mixup-DA for the broken rotor bar system (0.042 and 0.037 versus 0.059 and 0.046, respectively), despite achieving worse classification accuracy. This confirms that distributional proximity alone does not guarantee discriminative quality when the generative model fails to preserve fault-specific features. A similar pattern was observed for the rotor-bearing-disc system, where VAE and GAN produced lower MMD values than Mixup-DA and ACGAN but did not consistently translate this into higher classification accuracy. Regarding computational cost, Mixup-DA was the fastest method across both systems, whilst VAE required the longest generation time due to the iterative training of the encoder-decoder architecture. EWT-SINDy occupied an intermediate position in execution time but outperformed all four baselines in distributional fidelity.

It should be noted that the lower MMD achieved by EWT-SINDy reflects, in part, the physics-informed inductive bias of the sparse dynamical model, which constrains synthetic trajectories to remain near the observed operating regime by construction.

5.4 Interpretability

Interpretability in the proposed EWT-SINDy framework is achieved by extracting sparse, physically meaningful equations from the data. For visual analysis, the coefficients of each term in the governing equations were first averaged across repeated

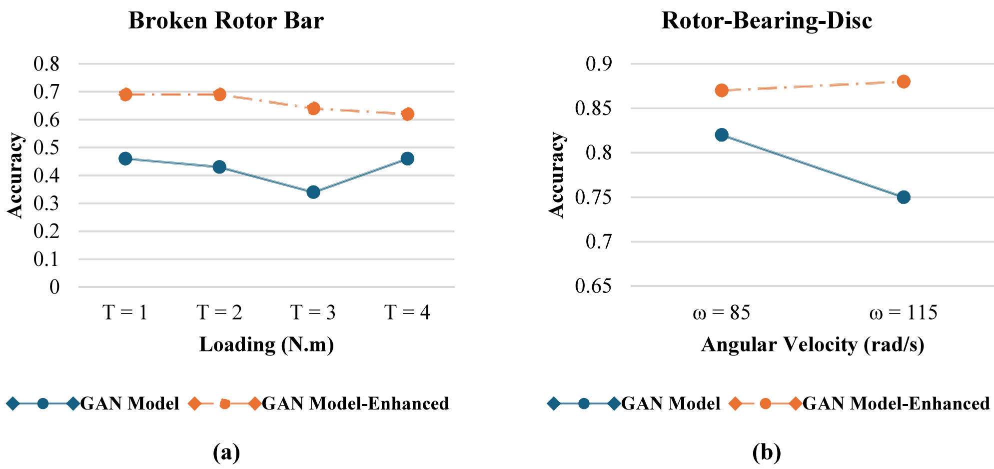

FIGURE 23
Fault diagnosis results utilising GAN data augmentation for **(a)** broken rotor bar and **(b)** rotor-bearing-disc systems.

TABLE 6 **Synthetic data quality and computational cost comparison.**

Case study	Method	MMD (x 10^{-2})	Generation time per condition (s)
Broken rotor bar	EWT-SINDy	0.013	41
Broken rotor bar	Mixup-DA	0.046	34.14
Broken rotor bar	ACGAN	0.037	58.31
Broken rotor bar	VAE	0.059	94.37
Broken rotor bar	GAN	0.042	87.23
Rotor-bearing-disc	EWT-SINDy	0.016	43.98
Rotor-bearing-disc	Mixup-DA	0.067	39.95
Rotor-bearing-disc	ACGAN	0.075	51.21
Rotor-bearing-disc	VAE	0.032	88.23
Rotor-bearing-disc	GAN	0.049	54.12

measurements for each health condition. These averaged coefficients were then gathered for every health state and plotted as violin plots to show their distribution and fault sensitivity. In each violin, the width represents the data density, the central line indicates the median, and the length captures the spread of the coefficients across different conditions (Rezazadeh et al., 2024).

5.4.1 Interpretation of extracted coefficients: broken rotor bar system

For the broken rotor bar system, violin plots were constructed for each of the 5 original state variables ($dx_1 - dx_5$), as illustrated in Figures 24a–e. In each plot, the x-axis labels ($c_1 - c_6$) represent the constant term and the 5 state variables in the corresponding equations. For example, in Figure 24a, the first violin labelled ' c_1' contains the set $[c_{1,rs}, c_{1,r1b}, c_{1,r2b}, c_{1,r3b}, c_{1,r4b}]$ from the equations for all health conditions.

Analysing Figure 24 reveals a clear diagonal structure in the coefficient matrices: for each state variable, the dominant coefficient is the self-coupling term (c_2 for dx_1, c_3 for dx_2, etc.), which is large, positive, and exhibits a narrow distribution. This confirms that each mode's own dynamics primarily govern its evolution. In contrast, most off-diagonal coefficients are tightly clustered near zero, indicating that cross-mode interactions are negligible, which is a direct result of the enforced sparsity and the physical independence of the extracted modes. Notably, certain coefficients (such as c_5 in multiple state variables) show greater spread or slight multimodality, reflecting increased sensitivity to rotor faults and providing clear statistical markers for condition monitoring and fault progression. This structure highlights both the interpretability and diagnostic relevance of the extracted models.

5.4.2 Interpretation of extracted coefficients: rotor-bearing-disc system

Figures 25a–h present violin plots for the 9 coefficients of the extracted equations of EWT for each of the 8 original state variables (like the previous case, the embedded state of variables were not

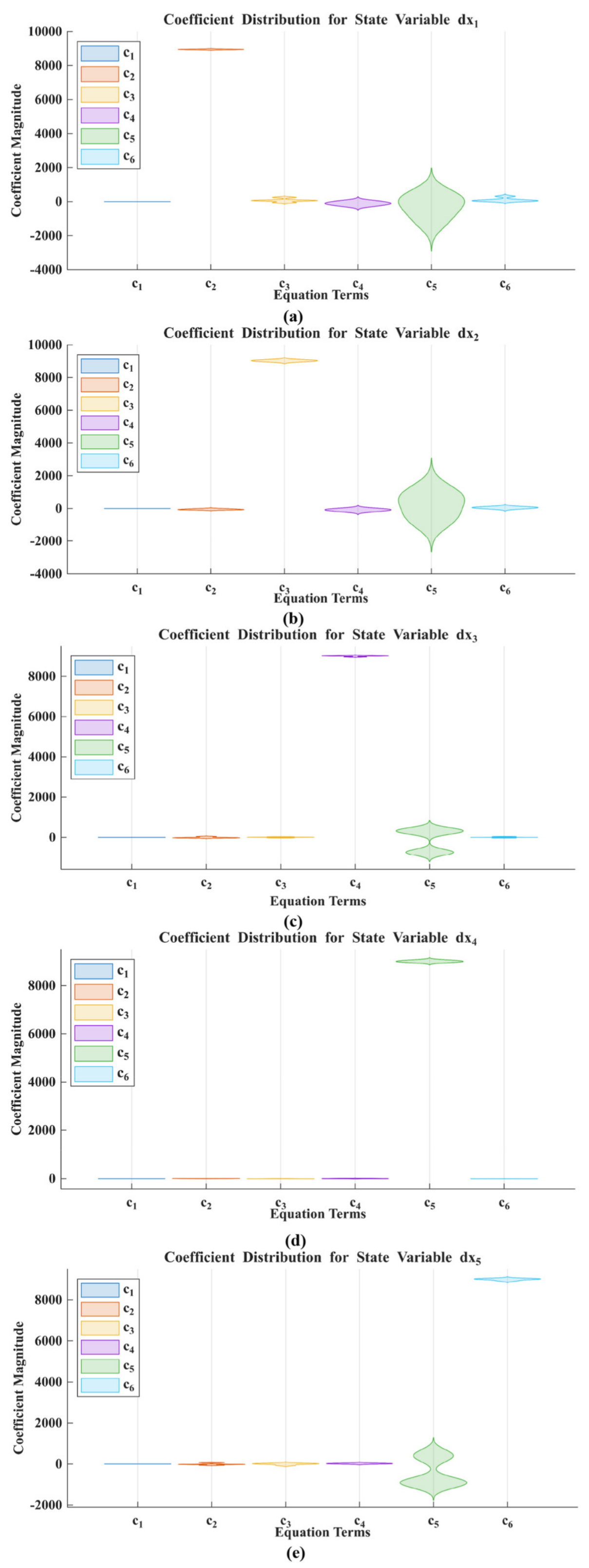

FIGURE 24
Violin plots of identified coefficients ($c_1 - c_6$) for the broken rotor bar system at T = 2 N m across different health conditions: **(a)** dx_1, **(b)** dx_2, **(c)** dx_3, **(d)** dx_4, **(e)** dx_5.

considered), corresponding to displacement measurements at bearings 1 and 2 in the transverse and rotational directions (see Figure 3). For each state variable, the coefficients were extracted for the normal, unbalanced, and misaligned rotor conditions and are plotted so that each violin displays the distribution of a given coefficient (c_k, k = 1: 9) across all 3 health states.

A close examination of these plots reveals that, in most directions and bearings, the self-coupling coefficients (c_2 for dx_1, c_3 for dx_2, up to c_9 for dx_8) consistently dominate, exhibiting high positive medians and narrow distributions across all health conditions. This diagonal dominance signifies that each sensor's displacement dynamics are primarily self-governed, confirming the independence of the measured degrees of freedom.

Importantly, the response to different fault types varies by sensor location and direction. In the rotational directions at bearing 2 (dx_7 and dx_8), as well as in certain transverse directions, the presence of misalignment or unbalance leads to a noticeable increase in both the spread and, in some cases, a shift in the median of specific cross-coupling coefficients, particularly c_7 and c_8. This broader distribution and shift under fault conditions are indicative of the heightened sensitivity of these axes to the corresponding faults, suggesting that the dynamic coupling and energy transfer are more pronounced in these measurement channels. In practice, monitoring the evolution of these fault-sensitive cross-coupling coefficients at bearing 2 could therefore provide an interpretable indicator of fault localisation and severity. Conversely, a number of off-diagonal coefficients remain tightly centred around zero, reinforcing the sparsity of the identified models and the weak cross-coupling between directions and bearings under all conditions.

Figure 25 demonstrates that fault effects in the rotor-bearing-disc system are not only detectable but are also localised to specific measurement channels and coefficients, with the most significant changes associated with the directions and bearings most physically exposed to the induced unbalance or misalignment. This precise, channel-specific response supports the effectiveness of the SINDy approach for interpretable and physically meaningful fault detection.

5.5 Computational efficiency

The proposed data synthesis architecture and fault detection methodology comprises multiple stages, as outlined previously. Two scripts were developed through MATLAB® R2024a: one for EWT-SINDy-based data augmentation and another for CNN training, validation, and testing. Whilst the EWT-SINDy code generated health scenario data across all conditions in a single execution, adjustments to input parameters were required for each loading case (broken rotor bar system) and angular velocity (rotor-bearing-disc system), necessitating separate runs per configuration. All computations were performed on a workstation with 32 GB RAM, a 4-core 2,800 MHz CPU, and an NVIDIA A10G GPU. Table 7 details execution times for data synthesis and CNN classification across loading and velocity conditions, with CNN training conducted exclusively on the GPU.

The prolonged execution times observed for the broken rotor bar system, as reflected in its larger dataset size, underscore the

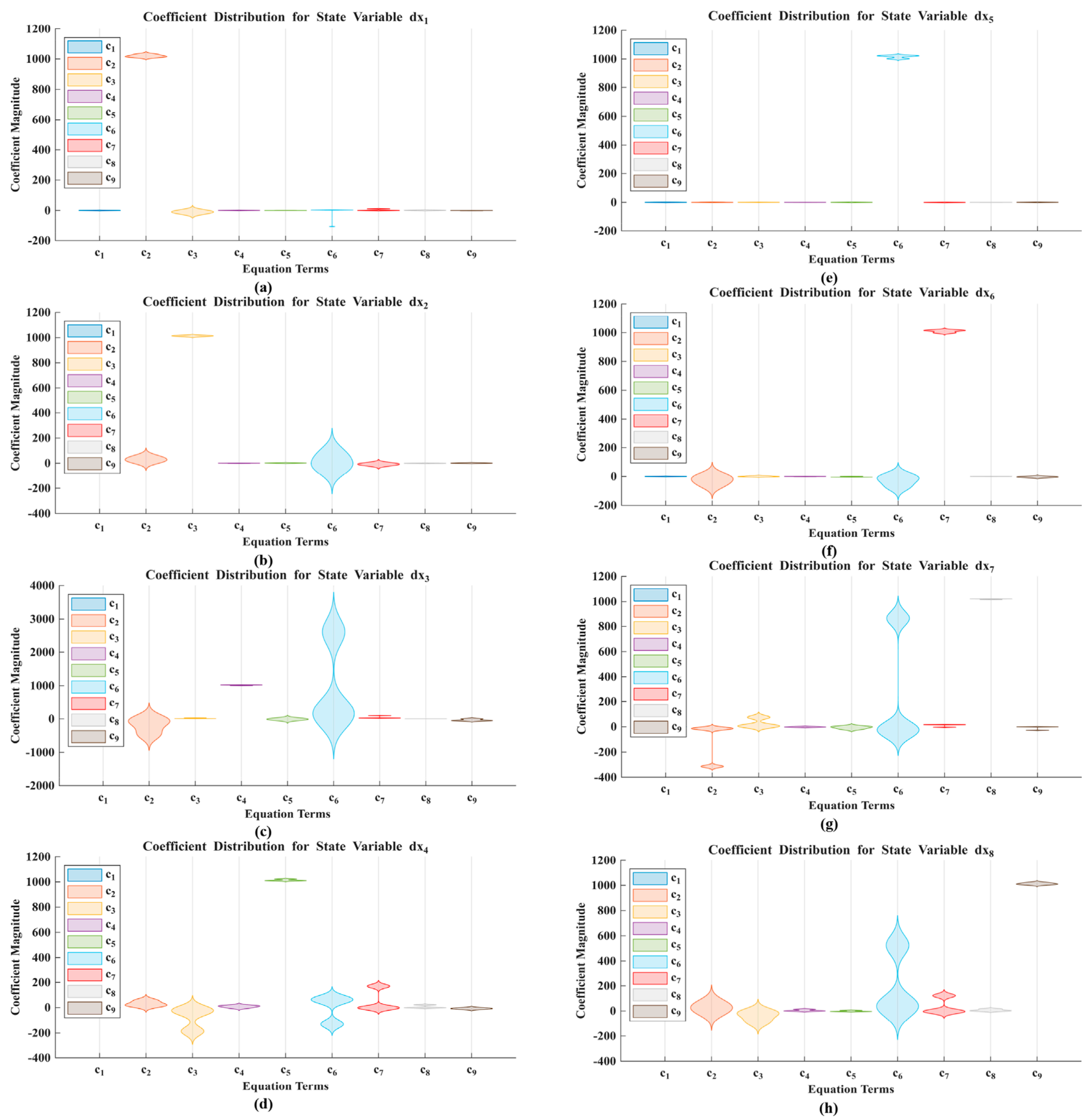

FIGURE 25
Violin plots of identified coefficients ($c_1 - c_9$) for the rotor-bearing-disc system at $\omega = 85$ rad/s across different health conditions: **(a)** dx_1, **(b)** dx_2, **(c)** dx_3, **(d)** dx_4, **(e)** dx_5, **(f)** dx_6, **(g)** dx_7, **(h)** dx_8.

computational demands imposed by increased data volumes. Despite the rotor-bearing-disc case study employing a greater number of sensor channels, it required significantly less time, highlighting the efficiency of the scheme when managing datasets with varying complexity and size. This discrepancy in execution times illustrates the framework's computational efficiency for the dataset sizes tested, suggesting reduced computational demands relative to dataset complexity. Such capabilities allow for the dynamic adjustment of computational resources based on the specific requirements of the dataset and operational context, thereby facilitating seamless integration into continuous monitoring systems without compromising performance. This adaptability ensures that the foundation can be effectively utilised in diverse industrial settings, where varying conditions may necessitate rapid adjustments to the computational strategies employed.

6 Discussion

Although the EWT-SINDy framework achieved high classification accuracy across the tested operating conditions, a small number of cases exhibited reconstruction or classification

TABLE 7 Execution time comparison across loading and angular velocity conditions.

Case study	EWT-SINDy execution time (s)	CNN execution time (s)
Broken rotor bar	164.00	242.74
Rotor-bearing-disc	87.95	26.80

difficulties that warrant closer examination. Understanding when and why the framework underperforms is important both for interpreting the results reported in Section 5 and for delineating the operational envelope within which the method can reliably be applied. The following discussion identifies the principal failure modes observed, the sample-size and noise conditions under which performance remained robust, and the contribution of each component of the pipeline to the overall outcome.

6.1 Failure modes and limitations

Analysis of the misclassified cases identified in Section 5.1, exemplified by observation 9 in the r4b class at T = 4 N m (Figure 11a), suggests specific conditions under which EWT-SINDy performance degrades. Qualitative inspection of the affected recordings indicated three recurring characteristics: (i) abrupt amplitude variations not representative of fault dynamics, which were consistent with inconsistent sensor mounting; (ii) non-stationary components that appeared to violate the quasi-periodic assumptions underlying EWT, attributable to transient disturbances during data acquisition; and (iii) short discontinuities consistent with measurement dropout or saturation. The reconstruction–original mismatch shown in Figure 11a illustrates how such anomalies propagate through the EWT-SINDy pipeline, in contrast to the close agreement obtained for a well-conditioned recording from the same class (Figure 11b). Across the experimental and numerical case studies, reconstruction failures of this kind were confined to a small minority of observations and were associated, on inspection, with identifiable acquisition anomalies rather than with limitations of the framework itself. This pattern indicates that the reconstruction stage of EWT-SINDy may, in addition to its augmentation role, provide a qualitative indicator of measurement quality, although a systematic evaluation of this secondary use lies beyond the scope of the present work.

6.2 Sample size requirements

Results demonstrate that a single observation per class suffices for majority-class identification (above 95% accuracy) under favourable SNR conditions (10 dB), whilst three observations improve robustness (over 98% accuracy) and reduce sensitivity to outlier measurements. The transition from one to three observations produced accuracy improvements of 0–5 percentage points across most operating conditions, with the largest gain (approximately 22 percentage points at the r4b class level under T = 4 N m) observed in the only condition for which the single-seed configuration produced misclassifications. This pattern is consistent with the acquisition anomalies discussed in Section 6.1 and indicates that additional seed observations primarily compensate for variability in individual recordings rather than improving performance under nominal conditions. A practical guideline follows: single observations may suffice for proof-of-concept work or high-quality laboratory data, whilst three to five observations provide redundancy against the recording-level variability typical of industrial deployments.

6.3 Sensitivity to noise levels

Although comprehensive SNR sweeps were not conducted, supplementary experiments at 5 dB and 15 dB SNR on a subset of conditions (T = 2 N m, all classes) indicated graceful degradation. At 15 dB, accuracy remained above 99%, whilst at 5 dB, performance decreased to 89%–92%, with primary degradation occurring in discrimination between adjacent fault severities (e.g., r2b vs. r3b). The EWT preprocessing step provides inherent noise resilience by isolating fault-sensitive frequency bands, but severe noise (SNR smaller than 5 dB) may require additional denoising preprocessing or ensemble-based approaches. The 10 dB level examined throughout this study represents a conservative estimate of typical industrial monitoring conditions based on prior literature.

6.4 Component-level ablation

To quantify the contribution of each component in the proposed framework, three ablated configurations were evaluated using the same CNN architecture and training protocol described in Section 5: (a) SINDy applied directly to the raw noisy signal without EWT pre-processing (SINDy-only), (b) EWT-filtered coefficients used to train the CNN without SINDy-based augmentation, relying solely on the available real observations (EWT-only), and (c) the full EWT-SINDy pipeline with time-delay embedding deactivated (EWT-SINDy-noTDE). All configurations used the single-seed setup at 10 dB SNR. Table 8 reports the classification accuracy for each configuration alongside the full framework across both the broken rotor bar and rotor-bearing-disc case studies.

The ablation results confirm that each component contributes measurably to the classification performance of the proposed framework. The SINDy-only configuration, which bypassed EWT pre-processing, produced the lowest accuracy across all conditions (40%–58.3%), demonstrating that SINDy cannot reliably identify governing dynamics from noisy, unfiltered signals, consistent with the reconstruction evidence presented in Figure 15. The EWT-only configuration, which relied solely on the available real observations without SINDy-based augmentation, improved accuracy to 62.2%–73.3%, indicating that EWT filtering alone provides useful fault-relevant features but that a single observation per class is insufficient for robust classifier training. The EWT-SINDy-noTDE configuration, in which time-delay embedding was deactivated, achieved accuracy between 77.8% and 91.7%, representing a

TABLE 8 Classification accuracy (%) for ablated configurations at 10 dB SNR (single-seed).

Configuration	Broken rotor bar			Rotor-bearing-disc		
	T = 1 N m	T = 2 N m	T = 3 N m	T = 4 N m	85 rad/s	115 rad/s
SINDy-only	46.7	48.9	51.1	40	58.3	58.3
EWT-only	71.1	73.3	71.1	62.2	73.3	70
EWT-SINDy-noTDE	82.2	80	84.4	77.8	91.7	86.7
EWT-SINDy (proposed)	100	100	100	95.6	98.3	100

substantial improvement over the single-component ablations but remaining consistently below the full framework. This performance gap confirms the role of time-delay embedding in enriching the state-space representation, as previously illustrated at the reconstruction level in Figure 6. Across both case studies, the full EWT-SINDy framework outperformed all ablated variants by margins ranging from 8 to 60 percentage points, demonstrating that the combination of adaptive signal decomposition, state-space embedding, and sparse dynamical modelling is necessary to achieve the reported classification performance under data-scarce, noisy conditions.

7 Conclusion

This paper introduced a data-efficient and interpretable framework for addressing data scarcity in rotating machinery fault diagnosis by integrating EWT, time-delay embedding, and SINDy. The approach extracts fault-relevant features through adaptive signal decomposition, identifies sparse governing equations, and generates synthetic training data via controlled perturbations of initial conditions.

Validation on an experimental broken-rotor-bar test rig and a numerical rotor-bearing-disc system showed that, with three real observations per fault class, the proposed framework achieved classification accuracies above 98% across loads of 1–4 N m and speeds of 85–115 rad/s at 10 dB SNR. The framework successfully generated synthetic data from as few as one to three real observations per fault class, indicating strong potential in settings where fault data acquisition is limited or costly.

Comparative analyses against four baseline methods (Mixup-DA, ACGAN, VAE, and GAN) showed that, under single-observation conditions, EWT-SINDy achieved accuracies of 95.6%–100%, whereas all baseline methods exhibited lower performance, with ACGAN and GAN particularly struggling in the broken rotor bar system under severely data-limited scenarios. This observed advantage underscores the benefit of physics-guided sparse modelling and adaptive empirical wavelet decomposition for few-shot augmentation. Furthermore, the interpretability of the sparse SINDy equations facilitates physical insight into fault progression and early identification of measurement-quality issues.

Despite these promising outcomes, several limitations remain. The method's sensitivity to the quality of the initial observations necessitates precise data acquisition and consistent sensor installation, as evidenced by isolated reconstruction failures. The framework has so far been validated only on rotary machinery; its applicability to other mechanical systems, fault types beyond those examined (unbalance, misalignment and broken bars) and different noise characteristics requires further investigation. Finally, although computational efficiency is satisfactory for the dataset sizes considered here, performance may not scale straightforwardly to higher-dimensional systems.

Future research directions include exploring advanced EWT schemes to enhance noise resilience beyond 10 dB SNR, refining SINDy for higher-noise environments and investigating integration with hybrid ML frameworks. Validation on diverse mechanical systems, including reciprocating machinery and industrial processes, would assess broader applicability. Extension to multi-fault scenarios, early fault detection, and real-time monitoring would demonstrate practical viability. Comparative studies with recent few-shot learning methods, including diffusion-based generative models, may result in insights into conditions favouring sparse dynamical modelling over purely data-driven augmentation.

Data availability statement

The raw data supporting the conclusions of this article will be made available by the authors, without undue reservation.

Author contributions

NR: Conceptualization, Data curation, Formal Analysis, Investigation, Methodology, Visualization, Writing – original draft, Writing – review and editing. AD: Methodology, Software, Supervision, Validation, Writing – review and editing. GL: Formal Analysis, Methodology, Validation, Writing – review and editing. FA: Investigation, Project administration, Writing – review and editing. MD: Conceptualization, Methodology, Project administration, Supervision, Writing – review and editing.

Funding

The author(s) declared that financial support was not received for this work and/or its publication.

Conflict of interest

The author(s) declared that this work was conducted in the absence of any commercial or financial relationships that could be construed as a potential conflict of interest.

Generative AI statement

The author(s) declared that generative AI was not used in the creation of this manuscript.

Any alternative text (alt text) provided alongside figures in this article has been generated by Frontiers with the support of artificial intelligence and reasonable efforts have been made to ensure accuracy, including review by the authors wherever possible. If you identify any issues, please contact us.

Publisher's note

References

Abdelhakim, B., Abderahim, A. A., and Djami, A. B. N. (2025). Use of statistical distance T2 and ARL to detect cutting tool drift. *Open J. Appl. Sci.* 15, 4335–4350. doi: 10.4236/ojapps.2025.1512279

Bai, X., Luo, Y., Jiang, L., Gupta, A., Kaveti, P., Singh, H., et al. (2024). Bridging the domain gap between synthetic and real-world data for autonomous driving. *ACM J. Aut. Transp. Syst.* 1, 1–15. doi: 10.1145/3633463

Bhadriraju, B., Kwon, J.S.-I., and Khan, F. (2022). "Prediction and isolation of process faults using operable adaptive sparse identification of systems (OASIS) and contribution plots," in *2022 American Control Conference (ACC)* (IEEE), 3626–3631.

Brunton, S. L., Proctor, J. L., and Kutz, J. N. (2016). Discovering governing equations from data by sparse identification of nonlinear dynamical systems. *Proc. Natl. Acad. Sci. U. S. A.* 113, 3932–3937. doi: 10.1073/pnas.1517384113

Cao, H., Shao, H., Liu, B., Cai, B., and Cheng, J. (2022). Clustering-guided novel unsupervised domain adversarial network for partial transfer fault diagnosis of rotating machinery. *IEEE Sens. J.* 22, 14387–14396. doi: 10.1109/JSEN.2022.3182727

Champion, K., Lusch, B., Nathan Kutz, J., and Brunton, S. L. (2019). Data-driven discovery of coordinates and governing equations. *Proc. Natl. Acad. Sci. U. S. A.* 116, 22445–22451. doi: 10.1073/pnas.1906995116

Conti, P., Kneifl, J., Manzoni, A., Frangi, A., Fehr, J., Brunton, S. L., et al. (2024). *VENI, Vindy, VICI: A Variational reduced-order Modeling Framework with Uncertainty Quantification.*

Das, O., Bagci Das, D., and Birant, D. (2023). Machine learning for fault analysis in rotating machinery: a comprehensive review. *Heliyon* 9, e17584. doi: 10.1016/j.heliyon.2023.e17584

Dixit, S., and Verma, N. K. (2020). Intelligent condition-based monitoring of rotary machines with few samples. *IEEE Sens. J.* 20, 14337–14346. doi: 10.1109/JSEN.2020.3008177

Djami, A. B. N., Nzie, W., and Sidibe, K. (2026). Optimization of the dependability of a hammer mill under budgetary constraints using evolutionary algorithms, stochastic methods, and statistical performance assessment. *Qual. Reliab. Eng. Int.* 42, 2289–2313. doi: 10.1002/qre.70196

Fallahy, S., and Rezazadeh, N. (2025). MARBLE-DA: masonry analysis with robust, batch-normalised, label-free, explainable domain adaptation for crack detection. *J. Build. Eng.* 116, 114673. doi: 10.1016/j.jobe.2025.114673

Faraji, F., Reza, M., and Kutz, J. N. (2025). Shallow recurrent decoder for reduced order modeling of $E \times B$ plasma dynamics. *Mach. Learn. Sci. Technol.* 6, 025024. doi: 10.1088/2632-2153/adcd20

Fasel, U., Kutz, J. N., Brunton, B. W., and Brunton, S. L. (2022). Ensemble-SINDy: robust sparse model discovery in the low-data, high-noise limit, with active learning and control. *Proc. R. Soc. A Math. Phys. Eng. Sci.* 478, 20210904. doi: 10.1098/rspa.2021.0904

Fathnejat, H., and Nava, V. (2025). Data augmentation for damaged scenarios in floating offshore wind turbines: an approach based on diffusion architecture, hierarchical variational approximation and healthy data distribution. *Eng. Comput.* 41, 1979–1999. doi: 10.1007/s00366-025-02148-6

Fung, L., Fasel, U., and Juniper, M. (2025). Rapid bayesian identification of sparse nonlinear dynamics from scarce and noisy data. *Proc. R. Soc. A Math. Phys. Eng. Sci.* 481, 20240200. doi: 10.1098/rspa.2024.0200

Gao, M. L., Williams, J. P., and Kutz, J. N. (2025). *Sparse Identification of Nonlinear Dynamics and Koopman Operators with Shallow Recurrent Decoder Networks.*

Gharehbaghi, V. R., Kalbkhani, H., Noroozinejad Farsangi, E., Yang, T. Y., and Mirjalili, S. (2023). A data-driven approach for linear and nonlinear damage detection using variational mode decomposition and GARCH model. *Eng. Comput.* 39, 2017–2034. doi: 10.1007/s00366-021-01568-4

Gilles, J. (2013). Empirical wavelet transform. *IEEE Trans. Signal Process.* 61, 3999–4010. doi: 10.1109/TSP.2013.2265222

Goodfellow, I., Pouget-Abadie, J., Mirza, M., Xu, B., Warde-Farley, D., Ozair, S., et al. (2020). Generative adversarial networks. *Commun. ACM.* 63, 139–144. doi: 10.1145/3422622

Hang, Q., Yang, J., and Xing, L. (2019). Diagnosis of rolling bearing based on classification for high dimensional unbalanced data. *IEEE Access* 7, 79159–79172. doi: 10.1109/ACCESS.2019.2919406

Huang, H. R., Li, K., Su, W. S., Bai, J. Y., Xue, Z. G., Zhou, L., et al. (2020). An improved empirical wavelet transform method for rolling bearing fault diagnosis. *Sci. China Technol. Sci.* 63, 2231–2240. doi: 10.1007/s11431-019-1522-1

Jiang, F., Lin, W., Wu, Z., Zhang, S., Chen, Z., and Li, W. (2024). Fault diagnosis of gearbox driven by vibration response mechanism and enhanced unsupervised domain adaptation. *Adv. Eng. Inf.* 61, 102460. doi: 10.1016/j.aei.2024.102460

Kingma, D. P., and Welling, M. (2019). An introduction to variational autoencoders. *Found. Trends® Mach. Learn.* 12, 307–392. doi: 10.1561/2200000056

Kumar, P., and Tiwari, R. (2024). Additive fault diagnosis techniques in rotor systems: a state-of-the-art review. *Sādhanā* 49, 207. doi: 10.1007/s12046-024-02543-7

Lee, J. D., Im, S., and Bang, H. (2024). "Data-driven fault detection and isolation for quadrotor using sparse identification of nonlinear dynamics and thau observer," in *2024 International Conference on Unmanned Aircraft Systems (ICUAS)* (IEEE), 382–389.

Leite, D., Andrade, E., Rativa, D., and Maciel, A. M. A. (2024). Fault detection and diagnosis in industry 4.0: a review on challenges and opportunities. *Sensors* 25, 60. doi: 10.3390/s25010060

Li, X., Zhang, W., Ding, Q., and Sun, J.-Q. (2020). Intelligent rotating machinery fault diagnosis based on deep learning using data augmentation. *J. Intell. Manuf.* 31, 433–452. doi: 10.1007/s10845-018-1456-1

Li, Q., Zhang, W., Chen, F., Huang, G., Wang, X., Yuan, W., et al. (2024a). Fault diagnosis of nuclear power plant sliding bearing-rotor systems using deep convolutional generative adversarial networks. *Nucl. Eng. Technol.* 56, 2958–2973. doi: 10.1016/j.net.2024.02.056

Li, Q., Chu, L., Sun, Q., Tang, Y., and Zhang, Y. (2024b). Fault identification of centrifugal pump using WGAN-GP method with unbalanced datasets based on kinematics simulation and experimental case. *Meas. Sci. Technol.* 35, 096108. doi: 10.1088/1361-6501/ad5222

Naozuka, G. T., Rocha, H. L., Silva, R. S., and Almeida, R. C. (2022). SINDy-SA framework: enhancing nonlinear system identification with sensitivity analysis. *Nonlinear Dyn.* 110, 2589–2609. doi: 10.1007/s11071-022-07755-2

Ngnassi Djami, A. B., and Abdelhakim, B. (2026). Integrated diagnosis and prognosis of dynamic systems using deep learning: case study on a welding robot. *IEEE Access* 14, 36737–36757. doi: 10.1109/ACCESS.2026.3671697

Ngnassi Djami, A. B., and Nzié, W. (2025). Meta-modeling of maintenance assets using an evolutionary algorithm approach: the case of a corn sheller. *Comput. Ind. Eng.* 209, 111485. doi: 10.1016/j.cie.2025.111485

Ngnassi Djami, A. B., Ngnassi Nguelcheu, U., and Nkongho Anyi, J. (2024a). Diagnosis and prognosis of soybean roaster failures using particle swarms. *Front. Mech. Eng.* 10, 1493579. doi: 10.3389/fmech.2024.1493579

Ngnassi Djami, A. B., Nzie, W., and Doka, S. Y. (2024b). Parameters estimation of the weibull law for reliability modeling of an equipment. *Life Cycle Reliab. Saf. Eng.* 13, 449–454. doi: 10.1007/s41872-024-00271-9

Pei, X., Su, S., Jiang, L., Chu, C., Gong, L., and Yuan, Y. (2022). Research on rolling bearing fault diagnosis method based on generative adversarial and transfer learning. *Processes* 10, 1443. doi: 10.3390/pr10081443

Piramoon, S., Ayoubi, M. A., and Bashash, S. (2024). Modeling and vibration suppression of rotating machines using the sparse identification of nonlinear dynamics and terminal sliding mode control. *IEEE Access* 12, 119272–119291. doi: 10.1109/ACCESS.2024.3449913

Qian, B., Cai, Y., Ran, Y., and Sun, W. (2024). Nonlinear mechanical response analysis and convolutional neural network enabled diagnosis of single-span rotor bearing system. *Sci. Rep.* 14, 10321. doi: 10.1038/s41598-024-61180-6

Radford, A., Metz, L., and Chintala, S. (2016). "Unsupervised representation learning with deep convolutional generative adversarial networks," in *4th International Conference on Learning Representations, ICLR 2016 - Conference Track Proceedings*.

Rezazadeh, N., de Oliveira, M., Perfetto, D., De Luca, A., and Caputo, F. (2023). Classification of unbalanced and bowed rotors under uncertainty using wavelet time scattering, LSTM, and SVM. *Appl. Sci. Switz.* 13, 6861. doi: 10.3390/app13126861

Rezazadeh, N., Perfetto, D., de Oliveira, M., De Luca, A., and Lamanna, G. (2024). A fine-tuning deep learning framework to palliate data distribution shift effects in rotary machine fault detection. *Struct. Health Monit.* 25, 661–683. doi: 10.1177/14759217241295951

Rezazadeh, N., Perfetto, D., Polverino, A., De Luca, A., and Lamanna, G. (2025). Guided wave-driven machine learning for damage classification with limited dataset in aluminum panel. *Struct. Health Monit.* 24, 3138–3161. doi: 10.1177/14759217241268394

Rezazadeh, N., De Luca, A., Lamanna, G., Annaz, F., and de Oliveira, M. (2026a). A novel interpretable domain adaptive framework for robust damage detection in composite structures under environmental variability. *Struct. Health Monit.*, 14759217261433879. doi: 10.1177/14759217261433879

Rezazadeh, N., Caputo, F., Aversano, A., Lamanna, G., De Luca, A., and Perfetto, D. (2026b). Prototype-attention domain adaptation for explainable bearing fault diagnosis. *Procedia Struct. Integr.* 80, 411–417. doi: 10.1016/j.prostr.2026.02.039

Rezazadeh, N., Lamanna, G., Caputo, F., De Oliveira, M., and De Luca, A. (2026c). Degradation mode identification and remaining useful life prediction via an interpretable CNN-BiLSTM framework. *Nondestruct. Test. Eval.*, 1–27. doi: 10.1080/10589759.2026.2660753

Shao, S., Wang, P., and Yan, R. (2019). Generative adversarial networks for data augmentation in machine fault diagnosis. *Comput. Ind.* 106, 85–93. doi: 10.1016/j.compind.2019.01.001

Tan, E., Algar, S., Corrêa, D., Small, M., Stemler, T., and Walker, D. (2023). *Selecting Embedding Delays: An Overview of Embedding Techniques and a New Method Using Persistent Homology*.

Torzoni, M., Manzoni, A., and Mariani, S. (2025). Enhancing Bayesian model updating in structural health monitoring via learnable mappings. *Eng. Comput.* 41, 4953–4975. doi: 10.1007/s00366-025-02224-x

Uhlig, S., Alkhasli, I., Schubert, F., Tschöpe, C., and Wolff, M. (2023). A review of synthetic and augmented training data for machine learning in ultrasonic non-destructive evaluation. *Ultrasonics* 134, 107041. doi: 10.1016/j.ultras.2023.107041

Wei, J., Huang, H., Yao, L., Hu, Y., Fan, Q., and Huang, D. (2020). New imbalanced fault diagnosis framework based on Cluster-MWMOTE and MFO-Optimized LS-SVM using limited and complex bearing data. *Eng. Appl. Artif. Intell.* 96, 103966. doi: 10.1016/j.engappai.2020.103966

Xiang, L., Zhang, X., Zhang, Y., Hu, A., and Bing, H. (2023). A novel method for rotor fault diagnosis based on deep transfer learning with simulated samples. *Measurement* 207, 112350. doi: 10.1016/j.measurement.2022.112350

Xin, Y., Li, S., Zhang, Z., An, Z., and Wang, J. (2019). Adaptive reinforced empirical morlet wavelet transform and its application in fault diagnosis of rotating machinery. *IEEE Access* 7, 65150–65162. doi: 10.1109/ACCESS.2019.2917042

Xu, B., Li, H., Ding, R., and Zhou, F. (2025). Fault diagnosis in electric motors using multi-mode time series and ensemble transformers network. *Sci. Rep.* 15, 7834. doi: 10.1038/s41598-025-89695-6

Yan, R., Shang, Z., Xu, H., Wen, J., Zhao, Z., Chen, X., et al. (2023). Wavelet transform for rotary machine fault diagnosis:10 years revisited. *Mech. Syst. Signal Process.* 200, 110545. doi: 10.1016/j.ymssp.2023.110545

Yu, K., Li, Y., Zhan, Q., Zhang, Y., and Xing, B. (2025). Intelligent fault diagnosis for cross-domain few-shot learning of rotating equipment based on mixup data augmentation. *Machines* 13, 807. doi: 10.3390/machines13090807

Zhang, Y., Du, X., Wen, G., Huang, X., Zhang, Z., and Xu, B. (2019a). An adaptive method based on fractional empirical wavelet transform and its application in rotating machinery fault diagnosis. *Meas. Sci. Technol.* 30, 035005. doi: 10.1088/1361-6501/aaf8e6

Zhang, W., Yang, D., Wang, H., Huang, X., and Gidlund, M. (2019b). CarNet: a dual correlation method for health perception of rotating machinery. *IEEE Sens. J.* 19, 7095–7106. doi: 10.1109/JSEN.2019.2912934

Zhang, N., Duan, L., Li, X., and Liu, X. (2023a). *Imbalanced Fault Diagnosis of Planetary Gearboxes Based on Noise Enhancement and Threshold Adaptive Siamese Decoupled Network*. IEEE International Conference on Prognostics and Health Management. ICPHM 2023.

Zhang, Q., He, Q., Qin, J., and Duan, J. (2023b). Application of fault diagnosis method combining finite element method and transfer learning for insufficient turbine rotor fault samples. *Entropy* 25, 414. doi: 10.3390/e25030414

Zhao, Z., Zhou, R., and Dong, Z. (2019). "Aero-engine faults diagnosis based on K-means improved Wasserstein GAN and relevant vector machine," in *Proceedings of the 2019 Chinese Control Conference* (CCC) (Piscataway, NJ: IEEE). 4795–4800. doi: 10.23919/ChiCC.2019.8865682

Zhao, S., Cheng, C., Lin, M., and Peng, Z. (2024a). Detection of breathing cracks using physics-constrained hybrid network. *Int. J. Mech. Sci.* 281, 109568. doi: 10.1016/j.ijmecsci.2024.109568

Zhao, Z., Xu, Y., Zhang, J., Zhao, R., Chen, Z., and Jiao, Y. (2024b). A semi-supervised gaussian mixture variational autoencoder method for few-shot fine-grained fault diagnosis. *Neural Netw.* 178, 106482. doi: 10.1016/j.neunet.2024.106482

Zhao, Z., Zhao, R., and Jiao, Y. (2024c). Random convolution layer: an auxiliary method to improve fault diagnosis performance. *J. Intell. Manuf.* 36, 4845–4866. doi: 10.1007/s10845-024-02458-4

Zheng, J., Pan, H., Yang, S., and Cheng, J. (2017). Adaptive parameterless empirical wavelet transform based time-frequency analysis method and its application to rotor rubbing fault diagnosis. *Signal Process.* 130, 305–314. doi: 10.1016/j.sigpro.2016.07.023

Zheng, L., Xiang, Y., and Luo, N. (2024). Nonlinear dynamic modeling and vibration analysis for early fault evolution of rolling bearings. *Sci. Rep.* 14, 23687. doi: 10.1038/s41598-024-75126-5

Zhu, H., and Fang, T. (2024). Compound fault diagnosis of rolling bearings with few-shot based on DCGAN-RepLKNet. *Meas. Sci. Technol.* 35, 066105. doi: 10.1088/1361-6501/ad24b5